

## Article

# Active Sites in H-Mordenite Catalysts Probed by NMR and FTIR

Marina G. Shelyapina <sup>1,\*</sup> , Ekaterina A. Krylova <sup>1</sup>, Anton S. Mazur <sup>2</sup>, Alexey A. Tsyganenko <sup>3</sup>, Yaroslav V. Shergin <sup>3</sup>, Elizaveta A. Satikova <sup>3</sup> and Vitalii Petranovskii <sup>4</sup> 

<sup>1</sup> Department of Nuclear Physics Research Methods, Saint Petersburg State University, 7/9 Universitetskaya Nab., 199034 Saint Petersburg, Russia

<sup>2</sup> Center for Magnetic Resonance, Saint Petersburg State University, 7/9 Universitetskaya Nab., 199034 Saint Petersburg, Russia

<sup>3</sup> Department of Photonics, Saint Petersburg State University, 7/9 Universitetskaya Nab., 199034 Saint Petersburg, Russia

<sup>4</sup> Centro de Nanociencias y Nanotecnología, Universidad Nacional Autónoma de México, Ensenada 22800, Baja California, Mexico

\* Correspondence: marina.shelyapina@spbu.ru

**Abstract:** Mordenites are widely used in catalysis and environmental protection. The catalytic properties of mordenite are largely determined by the composition of its crystal framework, i.e., the SiO<sub>2</sub>/Al<sub>2</sub>O<sub>3</sub> molar ratio (MR), and the cationic form. In H-mordenites, the most important characteristic becomes the structure and distribution of acid sites, which depends on the number and distribution of Al tetrahedra in the framework. In the present work, the local structure of these centers in H-mordenite catalysts with a nominal MR varied from 9.9 to 19.8 was studied in detail using a combination of magic angle spinning nuclear magnetic resonance (MAS NMR) and Fourier transform infrared spectroscopy (FTIR). <sup>27</sup>Al MAS NMR indicates the presence of extra-framework Al in most of the studied samples that results in a higher real MR of the zeolitic framework compared to the nominal value. Concentrations of Lewis and Brønsted acid sites, as well as of silanol groups were estimated by elemental analysis, NMR, and FTIR spectroscopy. The values of site concentrations obtained from band intensities of adsorbed CO and those of OH groups are compared with the amount of framework and extra-framework aluminum. The advantages and restrictions of different methods of active site characterization are discussed.

**Keywords:** H-mordenite; extra-framework Al; acid sites; NMR; FTIR; CO absorption



**Citation:** Shelyapina, M.G.; Krylova, E.A.; Mazur, A.S.; Tsyganenko, A.A.; Shergin, Y.V.; Satikova, E.A.; Petranovskii, V. Active Sites in H-Mordenite Catalysts Probed by NMR and FTIR. *Catalysts* **2023**, *13*, 344. <https://doi.org/10.3390/catal13020344>

Academic Editor: Roman Bulánek

Received: 25 December 2022

Revised: 16 January 2023

Accepted: 1 February 2023

Published: 3 February 2023



**Copyright:** © 2023 by the authors. Licensee MDPI, Basel, Switzerland. This article is an open access article distributed under the terms and conditions of the Creative Commons Attribution (CC BY) license (<https://creativecommons.org/licenses/by/4.0/>).

## 1. Introduction

Zeolites are crystalline aluminosilicates with open three-dimensional frameworks constructed of [SiO<sub>4</sub>]<sup>4-</sup> and [AlO<sub>4</sub>]<sup>5-</sup> tetrahedra connected to each other by oxygen bridges to form regular intracrystalline cavities and channels, where the extra-framework cations (such as Na<sup>+</sup>, K<sup>+</sup>, NH<sub>4</sub><sup>+</sup>, Ca<sup>2+</sup>, etc.), which compensate the negative charge of the framework are located [1]. Depending on the structural type, the size of the formed voids varies from 0.3 to 1.0 nm [2]. Due to their unique structural and chemical properties, such as ion exchange, developed inner surface, etc., that are vital for a wide range of industries, interest in zeolites does not weaken [3]. The two main applications of zeolites as molecular sieves and ion exchangers have made natural zeolites the most sought minerals on the market [4]. Until recently, synthetic zeolites have dominated the field of catalysis [5,6]. Current tendencies in the development of zeolites and zeolite-based materials include the adaptation of their properties, such as cationic composition [7,8], porosity [9–11], acidity [12–14] for a specific application, which, in addition to being used in catalysis, involves their use as adsorbents, biocides, as platforms for supporting active components in medicine and pharmacy, etc. [15–19].

Mordenite belongs to the so-called “big five” zeolites (ZSM-5, beta-zeolite, mordenite, faujasite, and ferrierite), which are widely used in industry as catalysts [20]. It crystallizes in an orthorhombic lattice with a system of main channels (formed by 12-membered rings,  $0.7 \times 0.65$  nm) and small channels (formed by 8-membered rings,  $0.57 \times 0.26$  nm) oriented along the *c*-axis and interconnected through side pockets [2]. The structure of mordenite is stable in a fairly wide range of  $\text{SiO}_2/\text{Al}_2\text{O}_3$  molar ratios (MR) (from 10 to  $\infty$ ). A change in the Al content while keeping the framework topology results in very strong differences in properties associated with changes in the arrangement of cation exchange centers ( $[\text{AlO}_4]^{5-}$  tetrahedra), not counting the generation of various kinds of defects in it, which determines the observed changes in properties [21–24]. The presence of different types of channel systems with available Brønsted acid sites determines the wide applicability of mordenite in various catalytic reactions such as synthesis and separation of hydrocarbons [25,26], dehydration of methanol [27], de- $\text{NO}_x$  catalysis [28,29], etc. It is also used as a form-selective catalyst [30,31].

Catalytic properties of mordenites are essentially governed by their MR [23,24]. A study of acidity over a wide range of  $\text{SiO}_2/\text{Al}_2\text{O}_3$  molar ratios (from 10 to 206) [32] showed a volcano-shape dependence of mordenite acidity on the  $\text{SiO}_2/\text{Al}_2\text{O}_3$  value. The ammonia desorption peak temperature can be considered a measure of the strength of the acid sites. A decrease in the peak temperature in spectra of temperature-programmed desorption of ammonia correlates with a decrease in acid strength [33]. Maximum acidity was observed for the sample with MR = 15, followed by MR = 20 [32]. Similarly, studies of copper-exchanged mordenite obtained from this set of protonated mordenites showed that the maximum acidity value and the strongest acid centers were present in the mordenite with MR = 15, confirming the importance of these acid centers in various processes. Thus, the transition from the change in acidity increase with increasing MR to the decrease in acidity with its further growth occurs exactly in the range from 10 to 20, which causes interest in a detailed study of the processes occurring in the structure of mordenite.

Studies in a wide range of MR from 10 to 206 of copper-exchanged mordenites obtained from a protonated form have shown that the maximum value of acidity and the strongest acid centers are present in mordenite with MR = 15 [23]. However, the reasons for such selectivity are still unclear, but they can be associated with Brønsted acid site locations. A comprehensive Fourier transform infrared (FTIR) study of protonated mordenites prepared from industrial Na mordenites with MR = 14.6 by treatment in  $\text{NH}_4\text{NO}_3$  solution followed by calcination demonstrated the existence of at least six distinct Brønsted acid sites [34]. For the purely acidic H-mordenite sample they found the following distribution between the Brønsted acid sites localization: in the small channels (25%), in the intersections between the side pockets (~13%), and the rest in the main channels.

In addition, the properties of protonated zeolites in general, and mordenites in particular, depend on the synthesis method [35–38]. Our recent study of two H-mordenites with MR close to 15, but synthesized in two different ways: by acid etching and from  $\text{NH}_4$ -form, showed an essential difference in sample topology, morphology, element distribution, and acid site [39].

In the present paper, we report the results of a comparative study of a wider set of mordenite samples with MR varied from 9.9 to 19.8 that was carried out by various techniques, including nuclear magnetic resonance (NMR) and FTIR spectroscopy, two complementary methods that provide information about the local structure of the studied materials.

## 2. Results and Discussion

A set of samples of protonated mordenite manufactured by TOSOH Co., Tokyo, Japan, with nominal  $\text{SiO}_2/\text{Al}_2\text{O}_3$  ratios of 9.9, 15.0, 15.2, 15.7, 15.8, 18.7, and 19.8, respectively, was studied. Further in the work, the samples will be referred to as H-MOR-*X*, where *X* is the corresponding nominal MR of the sample.

### 2.1. Elemental Analysis

Since heterogeneous catalytic reactions take place on surface sites, studies of the distribution of active centers on the catalyst surface are of great importance. However, the distribution of elements in a zeolite catalyst crystal is usually inhomogeneous [40]. From this point of view, for a more complete understanding of the elemental composition of the sample, it is necessary to apply complementary methods with different depth vision: X-ray photoelectron spectroscopy (XPS) that provides information on the penetration depth between 1 and 10 nm [41], energy dispersive spectroscopy (EDS) with deeper vision, up to 1000 nm [42], and inductively coupled plasma—optical emission spectroscopy (ICP-OES) that provides information about the gross composition of the substance.

The SiO<sub>2</sub>/Al<sub>2</sub>O<sub>3</sub> ratio for the studied samples as determined by the XPS, EDS, and ICP-OES methods, is listed in Table 1. The original ICP-OES data for element composition (Si, Al, and Na content) are given in Supplementary Materials, Table S1. As one can see, MR for the bulk as determined from ICP-OES systematically underestimate the nominal value by about 10%, whereas XPS for all the samples, except for H-MOR-18.7, shows a noticeably higher MR, which may essentially exceed the nominal value. EDS provides intermediate values closer to bulk ICP-OES, which is correlate with its penetration depths. Such a discrepancy between the bulk and surface composition is issued by inhomogeneity of the Al distribution over the depth of the sample crystals, especially for the samples in the middle of the studied MR range: all the samples, except H-MOR-18.7, for which the element distribution is quite uniform, dealumination is observed on the surface, most clearly pronounced for H-MOR-15.2, H-MOR-15.7, and H-MOR-15.8. The problem of such diversity can be related to the sample preparation method.

**Table 1.** SiO<sub>2</sub>/Al<sub>2</sub>O<sub>3</sub> ratio of the studied samples determined by different methods.

Sample	XPS	EDS	ICP-OES	NMR ( <sup>27</sup> Al) <sup>1</sup>	NMR ( <sup>29</sup> Si) <sup>1</sup>
H-MOR-9.9	10.8 ± 0.3	9.3 ± 0.5	8.72 ± 0.09	9.9 ± 0.1	10.4 ± 0.2
H-MOR-15.0	14.4 ± 0.2	14.3 ± 0.9	13.94 ± 0.14	14.3 ± 0.2	16.0 ± 0.3
H-MOR-15.2	21.4 ± 0.4	14.4 ± 0.7	13.38 ± 0.14	18.1 ± 0.2	17.8 ± 1.0
H-MOR-15.7	24.9 ± 0.2	15.1 ± 0.9	13.63 ± 0.16	18.2 ± 0.2	21.0 ± 1.0
H-MOR-15.8	21.2 ± 0.3	14.5 ± 0.8	14.06 ± 0.14	18.2 ± 0.2	23.0 ± 1.0
H-MOR-18.7	16.5 ± 0.4	17.6 ± 0.9	16.67 ± 0.17	18.5 ± 0.2	20.5 ± 0.8
H-MOR-19.8	21.6 ± 0.4	19.3 ± 0.9	17.61 ± 0.18	18.2 ± 0.2	15.8 ± 0.5

<sup>1</sup> For details see Section 2.5.

According to the ICP-OES data, there is a slight admixture of Na in the H-MOR-15.2 and H-MOR-15.7 samples (Na/Al = 0.09 and 0.07, respectively), which may indirectly indicate the method of sample synthesis. The samples were supplied by TOSOH, Japan, and the details of their synthesis are unknown. However, one can assume that, at least for these two samples, the H-mordenites were obtained from the original Na form.

### 2.2. X-ray Diffraction Studies

Powder X-ray diffraction (XRD) patterns of the studied H-MOR series are shown in Figure 1a. The XRD analysis confirms that all the samples retain the mordenite crystalline structure, and no peaks corresponding to other phases are observed. The lattice parameters for the studied samples, as well as the unit cell volume, are listed in Table 2. As can be seen from Table 2, the *c* parameter changes slightly and monotonously decreases with MR increasing, whereas the changes in *a* and *b* look rather sporadic. However, if one introduces the so-called contraction parameter  $K = a/b$ , which reflects the contraction of the main mordenite channel [36,43], one can see, in Figure 1b, that for the samples H-MOR-15.2, H-MOR-15.7, H-MOR-15.8 the *K* parameter is out of the general trend and is essentially higher comparing to the rest of the samples. This indicates a change in the shape of channels in the samples with the corresponding MR, which may be a consequence of the different arrangement of Al tetrahedra, and, accordingly, compensating cations and/or Brønsted

acid sites the zeolite structure, or relatively high amount of extra-framework Al, as it will be shown in Section 2.5.1.

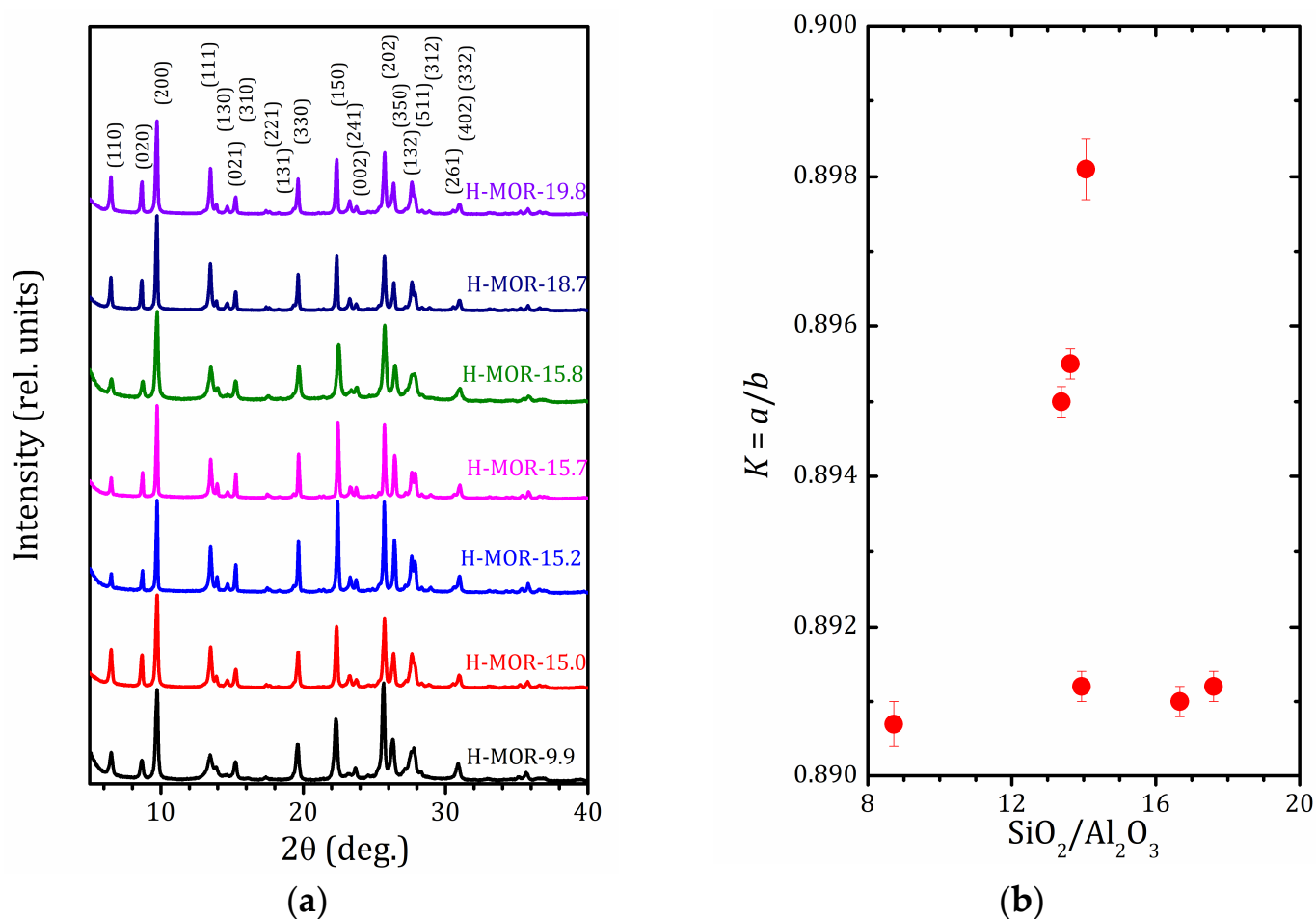


**Figure 1.** Powder XRD patterns for the studied samples (a) and the contraction parameter  $K = a/b$  plotted versus MR as determined by ICP-OES (b).

**Table 2.** X-ray lattice parameters, unit cell volume, a/b ratio for the studied samples.

Sample	Lattice Parameters (Å)			Unit Cell Volume (Å <sup>3</sup> )	$K = a/b$
	<i>a</i>	<i>b</i>	<i>c</i>		
H-MOR-9.9	18.194 ± 0.003	20.425 ± 0.003	7.521 ± 0.001	2794.8 ± 0.8	0.8907 ± 0.3
H-MOR-15.0	18.152 ± 0.002	20.368 ± 0.002	7.491 ± 0.001	2769.7 ± 0.5	0.8912 ± 0.2
H-MOR-15.2	18.161 ± 0.002	20.292 ± 0.002	7.493 ± 0.001	2761.4 ± 0.4	0.8950 ± 0.2
H-MOR-15.7	18.149 ± 0.002	20.267 ± 0.002	7.487 ± 0.001	2754.1 ± 0.3	0.8955 ± 0.2
H-MOR-15.8	18.182 ± 0.004	20.245 ± 0.004	7.489 ± 0.002	2756.5 ± 0.9	0.8981 ± 0.4
H-MOR-18.7	18.112 ± 0.002	20.327 ± 0.002	7.481 ± 0.001	2754.2 ± 0.4	0.8910 ± 0.2
H-MOR-19.8	18.133 ± 0.002	20.346 ± 0.002	7.481 ± 0.001	2760.1 ± 0.4	0.8912 ± 0.2

### 2.3. SEM Studies

The morphology of the samples was studied by scanning electron microscopy (SEM). SEM images for the studied samples are shown in Figure 2. The studied samples can be classified into two groups according to their morphology. The crystallite shape of the majority of the samples (H-MOR-9.9, H-MOR-15.0, H-MOR-15.8, H-MOR-18.7, H-MOR-19.8) can be described as individual crystals in the form of fibers, the length of which varies from 200 to 800 nm, combined in parallel into agglomerates ranging in size from 400 nm to 10 microns. However, two samples stand out from the overall picture, namely H-MOR-15.2

and H-MOR-15.7. SEM images evidence crystallites in a form of plates of several  $\mu\text{m}$  that form a “shell” with a size of 20–100  $\mu\text{m}$ . Such a morphology is probably related to the different methods of synthesis of these two samples (we remind that the presence of Na was detected by ICP-OES).

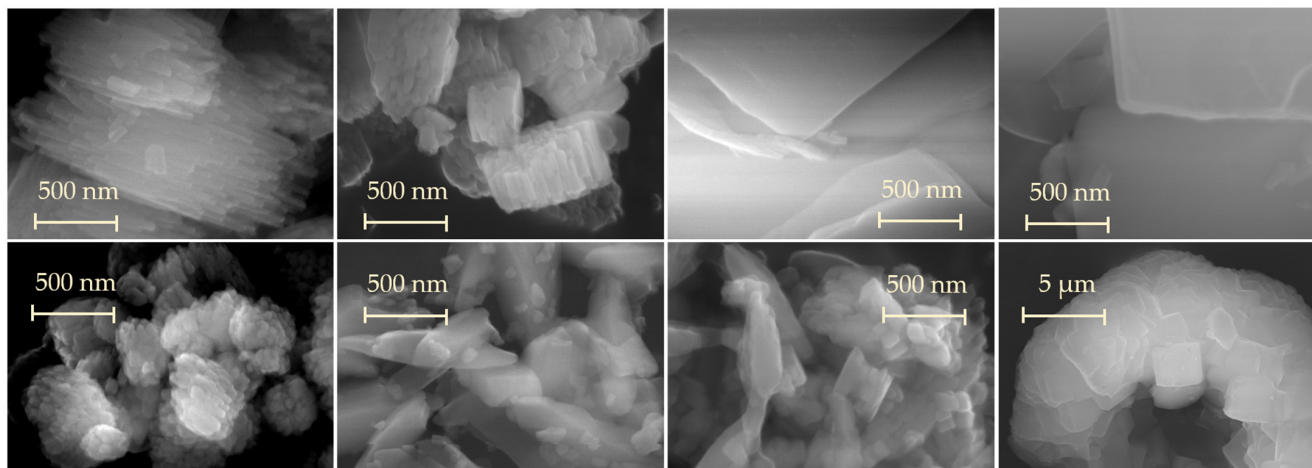


**Figure 2.** SEM images of the samples. Upper row from left to right: H-MOR-9.9, H-MOR-15.0, H-MOR-15.2 and H-MOR-15.7; lower row from left to right: H-MOR-15.8, H-MOR-18.7, H-MOR-19.8, and H-MOR-15.7 in a larger scale.

#### 2.4. Thermogravimetric Analysis

Figure 3a shows the thermogravimetric (TG) curves for all the studied samples. For the convenience of data analysis, typical differentiated TG (DTG) curves are shown in Figure 3b. As one can see, the total mass loss within the studied temperature range noticeably varies from sample to sample, without any correlation with the MR ratio, but the samples can be divided into two groups according to the shape of the TG curve.

The first group that includes H-MOR-15.2, H-MOR-15.7, H-MOR-15.8, and H-MOR-18.7 exhibits a sharp mass loss below 250 °C that can be divided into two Gaussian peaks on DTG associated with water release from the main mordenite channel (below 100 °C), and from side pockets (between 100 and 250 °C) [44] (the low water content for H-MOR-18.7 may be associated with partial destruction of the mordenite framework during post-synthesis treatment [29,30]). However, even above 250 °C, a linear mass loss is observed, which is not reflected in DTG and is related to the dehydroxylation [43]. H-MOR-15.8 demonstrates the greatest slope of the TG curve in this temperature range, which points out the presence of the largest amount of hydroxyls. The other samples, H-MOR-9.9, H-MOR-15.0, and H-MOR-19.8, in addition to the water release below 250 °C, simultaneously with the slope of the TG curve associated with dihydroxylation, show an additional peak on DTG that can be attributed to the ammonium decomposition [39]. The latter was confirmed by IR spectroscopy and NMR data, see Sections 2.5 and 2.6.

#### 2.5. NMR Characterization

##### 2.5.1. $^{27}\text{Al}$ and $^{29}\text{Si}$ MAS NMR

It is known that the methods used to synthesize H-form zeolites are often quite invasive and result in a partial collapse of the framework [45]. To estimate a share of extra-framework aluminum, we used  $^{27}\text{Al}$  MAS NMR spectroscopy. The spectra shown in Figure 4a indicate that the majority of Al are in regular tetrahedral framework sites (a signal at about 57 ppm); however, for almost all samples, a signal appears at approximately 0 ppm that corresponds to the extra-framework octahedral Al.

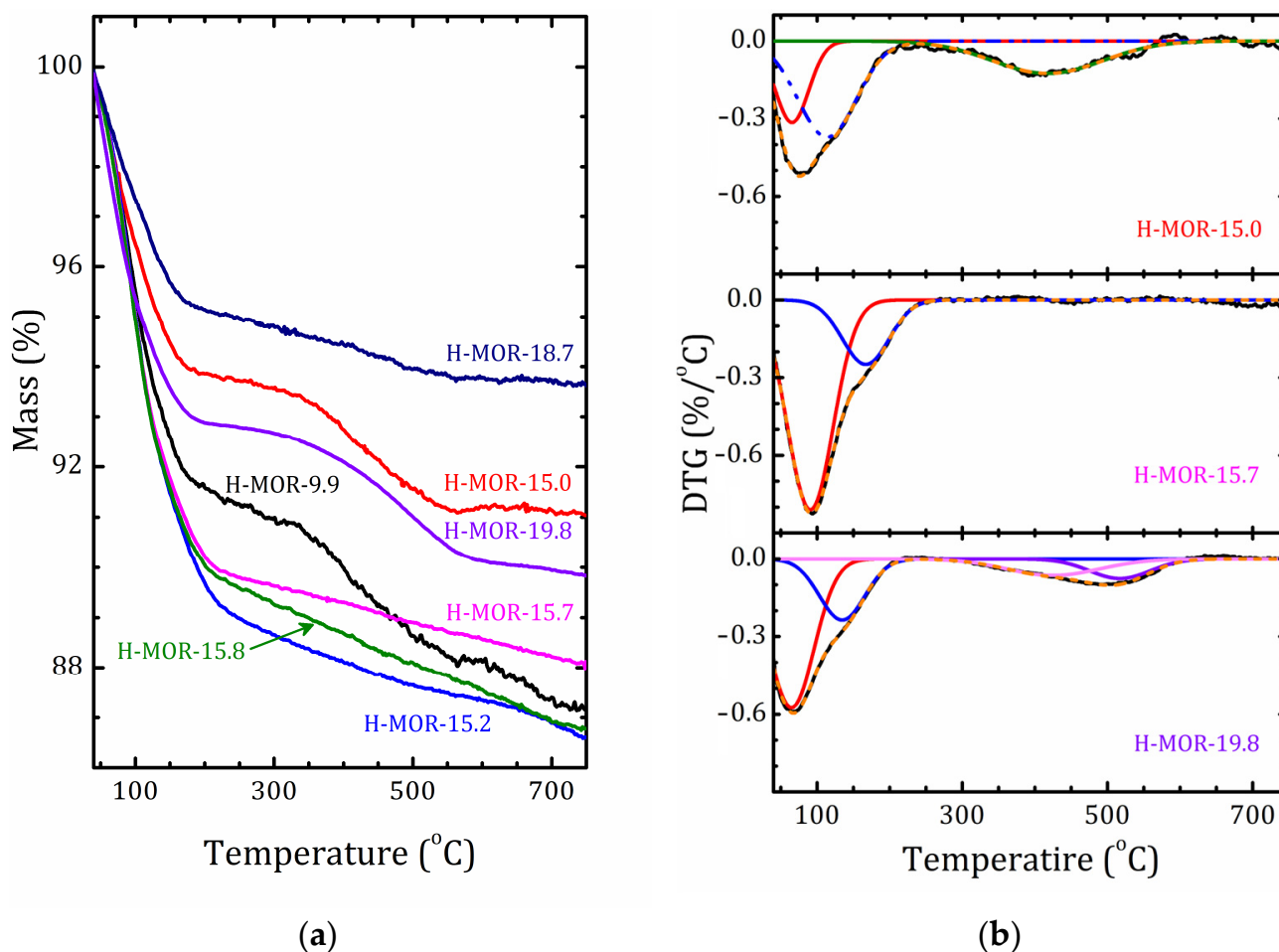


**Figure 3.** TG curves for all studied samples (a) and DTG curves with their decomposition for H-MOR-9.9, H-MOR-15.7, and H-MOR-19.8 (b).

The strongest signals of extra-framework Al, about 25% of total intensity, are observed for the samples H-MOR-15.2, H-MOR-15.7, and H-MOR-15.8. It should be noted that for these samples the main  $^{27}\text{Al}$  signal is observed at 56 ppm, whereas for others at 57 ppm (H-MOR-9.9 and H-MOR-15.0), and at 58 ppm (H-MOR-18.9 and H-MOR-19.8), which can be related with a preparation method and, as a consequence, the local environment of  $\text{AlO}_4$  tetrahedra (the presence of  $\text{NH}_4^+$  cation will be discussed later). For H-MOR-19.8, an additional large signal is observed at 47 ppm. This signal can be attributed to four-coordinated aluminum sites ( $\text{Al}_{\text{tetra-II}}$ ), but with a strong quadrupole interaction [46,47] due to distortion of the  $\text{AlO}_4$  tetrahedra. Accounting for the quantity of extra-framework Al, we recalculated the  $\text{SiO}_2/\text{Al}_2\text{O}_3$  that can be attributed to the zeolite and listed it in Table 1 for easier comparison with the results obtained by other methods. It is interesting that, with the exception of H-MOR-9.9 and H-MOR-15.0, for all other samples, the corrected  $^{27}\text{Al}$  MAS NMR data results in a  $\text{SiO}_2/\text{Al}_2\text{O}_3$  ratio close to 18.

The  $^{29}\text{Si}$  MAS NMR spectra of the studied H-mordenite samples are shown in Figure 4b. The spectra can be well described by a superposition of a set of Gaussian lines (from two to four) centered at about  $-112$ ,  $-105$ ,  $-100$ , and  $-93$ , which can be assigned to the  $\text{Q}^4(n\text{Al})$  ( $n = 0, 1, 2$ , and  $3$ ) Si sites, for which the nearest environment (neighboring tetrahedra) contains  $n$  Al atoms, respectively [24]. The positions of individual spectral lines, as well as their integral intensities, are listed in Table 3. With increasing  $\text{SiO}_2/\text{Al}_2\text{O}_3$  (both nominal and determined by ICP-OES or corrected for  $^{27}\text{Al}$  NMR), one can see that, contrary to what is expected, a redistribution between the integral intensities of the  $\text{Q}^4(0\text{Al})$  and  $\text{Q}^4(1\text{Al})$  lines is not monotonous; the most obvious is a sharp increase in the contribution of  $\text{Q}^4(0\text{Al})$  with the complete absence of  $\text{Q}^4(2\text{Al})$  for H-MOR-18.7. Moreover, for H-MOR-18.7 and

H-MOR-19.8, an additional signal at about  $-114$  ppm is observed that is characteristic of high siliceous mordenites [48].

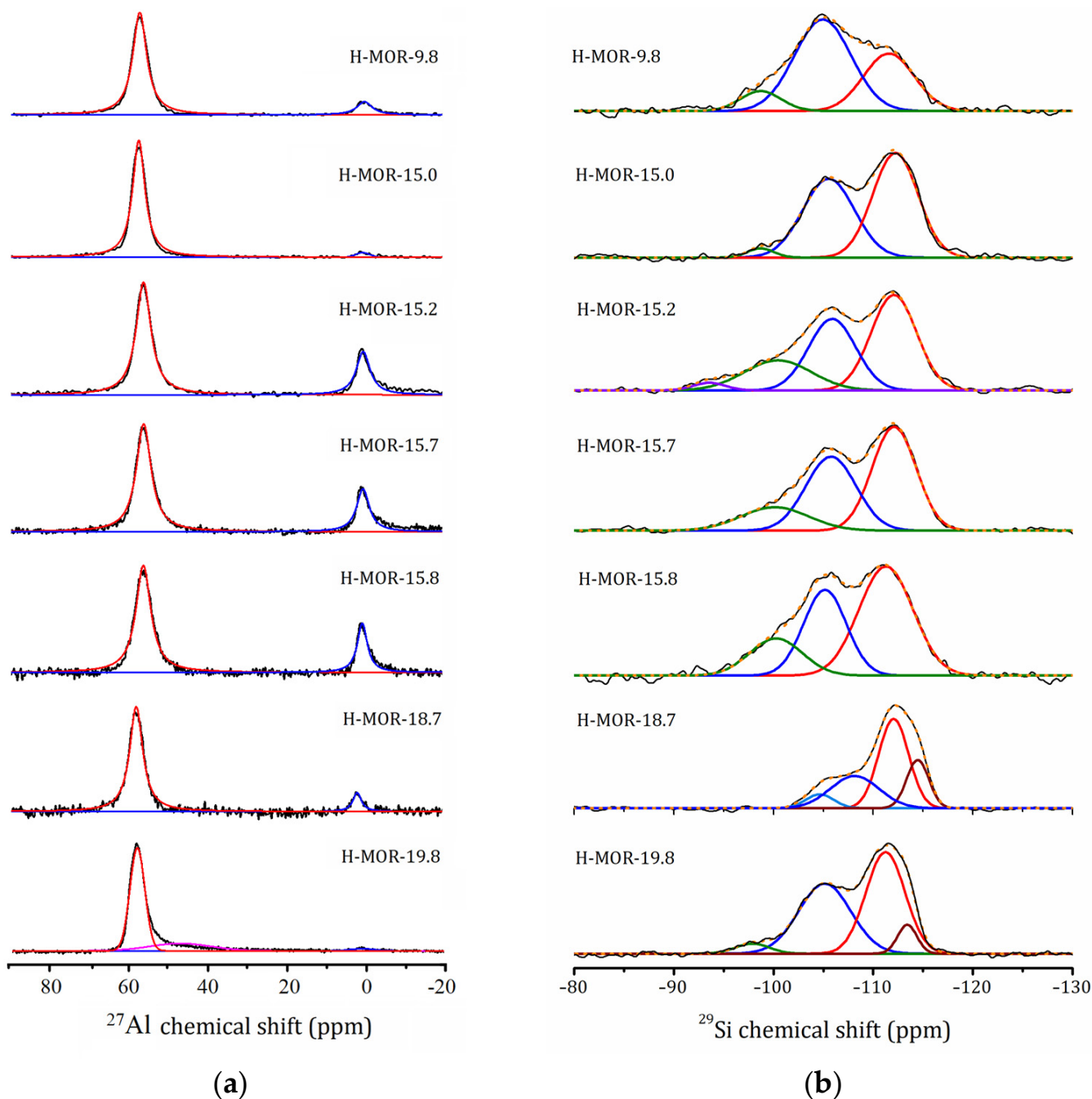


**Figure 4.**  $^{27}\text{Al}$  (a) and  $^{29}\text{Si}$  (b) MAS NMR spectra of the studied samples and their decomposition.

It is known that  $^{29}\text{Si}$  MAS NMR can also be used to determine the  $\text{SiO}_2/\text{Al}_2\text{O}_3$  ratio related directly to the zeolite framework [49]. Assuming the Löwenstein rule [50], which was deduced from electrostatic reasons and was proved recently within a more rigorous approach [51], according to which Al–O–Al bonds are not allowed, the  $\text{SiO}_2/\text{Al}_2\text{O}_3$  ratio can be estimated as follows [48]:

$$\frac{\text{SiO}_2}{\text{Al}_2\text{O}_3} = 2 \cdot \frac{\text{Si}}{\text{Al}} = 2 \cdot \frac{\sum_{i=0}^4 I_{\text{Q}^i(\text{nAl})}}{\sum_{i=0}^4 \frac{n}{4} (I_{\text{Q}^i(\text{nAl})})}, \quad (1)$$

where  $I_{Q^4(nAl)}$  is the peak areas of individual  $^{29}Si$  NMR lines attributed to  $Q^4(0Al)$ . However, for the H-MOR-15.2, H-MOR-15.7, and H-MOR-15.8 samples such an assignment results in a  $SiO_2/Al_2O_3$  value of half as much as compared to both nominal and determined by ICP-OES or corrected for  $^{27}Al$  NMR. It should be noted that the  $Q^4(2Al)$  signal in mordenite may overlap with  $Q^3(AlO)$  [52,53]. As it will be shown in Section 2.6, these samples demonstrate the presence of a large number of silanol groups, several times larger than other samples. This allows us to assume that for H-MOR-15.2, H-MOR-15.7, and H-MOR-15.8 the main contribution to the signal at  $-100$  ppm is not due to  $Q^4(2Al)$ , but  $Q^3(0Al)$  sites. The  $SiO_2/Al_2O_3$  ratios determined from  $^{29}Si$  NMR according to this assignment spectra are also listed in Table 1, and, as one can see, it is in reasonable agreement with the values determined by other methods.

**Table 3.** Relative integral intensities ( $I$ ) of individual lines  $^{29}Si$  and  $^{27}Al$  NMR spectra and  $^{29}Si$  isotropic chemical shifts ( $\delta_{iso}$ ) for the studied H-mordenite samples.

Site	Parameter	Sample						
		H-MOR-9.9	H-MOR-15.0	H-MOR-15.2	H-MOR-15.7	H-MOR-15.8	H-MOR-18.7	H-MOR-19.8
$Al_{tetra-I}$	$I$ (%)	$88 \pm 1$	$97 \pm 1$	$74 \pm 1$	$75 \pm 1$	$77 \pm 1$	$90 \pm 1$	$75 \pm 1$
$Al_{tetra-II}$	$I$ (%)	–	–	–	–	–	–	$22 \pm 1$
$Al_{octa}$	$I$ (%)	$12 \pm 1$	$3 \pm 1$	$26 \pm 1$	$23 \pm 1$	$23 \pm 1$	$10 \pm 1$	$3 \pm 1$
$Q^4(0Al)$ <sup>1</sup>	$\delta_{iso}$ (ppm)	–	–	–	–	–	$-114.5 \pm 0.1$	$-113.4 \pm 0.1$
	$I$ (%)	–	–	–	–	–	$16 \pm 1$	$6 \pm 1$
$Q^4(0Al)$	$\delta_{iso}$ (ppm)	$-111.6 \pm 0.1$	$-112.2 \pm 0.1$	$-112.1 \pm 0.1$	$-112.1 \pm 0.1$	$-111.3 \pm 0.1$	$-111.6 \pm 0.1$	$-111.6 \pm 0.1$
	$I$ (%)	$33 \pm 2$	$52 \pm 2$	$42 \pm 2$	$46 \pm 2$	$51 \pm 2$	$45 \pm 1$	$53 \pm 1$
$Q^4(1Al)$	$\delta_{iso}$ (ppm)	–	–	–	–	–	$-108.1 \pm 0.1$	–
	$I$ (%)	–	–	–	–	–	$28 \pm 1$	–
$Q^4(1Al)$	$\delta_{iso}$ (ppm)	$-104.9 \pm 0.1$	$-105.5 \pm 0.1$	$-105.9 \pm 0.1$	$-105.8 \pm 0.1$	$-105.2 \pm 0.1$	$-104.6 \pm 0.1$	$-105.1 \pm 0.1$
	$I$ (%)	$58 \pm 2$	$45 \pm 2$	$36 \pm 2$	$38 \pm 2$	$34 \pm 2$	$11 \pm 1$	$43 \pm 1$
$Q^4(2Al)$	$\delta_{iso}$ (ppm)	$-98.7 \pm 0.1$	$-98.7 \pm 0.1$	–	–	–	–	$-97.9 \pm 0.1$
	$I$ (%)	$9 \pm 3$	$3 \pm 1$	–	–	–	–	$4 \pm 1$
$Q^4(3Al)$	$\delta_{iso}$ (ppm)	–	–	$-93.5 \pm 0.1$	–	–	–	–
	$I$ (%)	–	–	$3 \pm 1$	–	–	–	–
$Q^3(0Al)$	$\delta_{iso}$ (ppm)	–	–	$-100.4 \pm 0.1$	$-100.1 \pm 0.1$	$-100.2 \pm 0.1$	–	–
	$I$ (%)	–	–	$19 \pm 1$	$16 \pm 1$	$15 \pm 2$	–	–

<sup>1</sup> For the high siliceous mordenite.

### 2.5.2. $^1H$ MAS NMR

$^1H$  MAS NMR spectra were acquired at a rotor frequency ( $\nu_{rot}$ ) of 15 kHz for the samples without any pretreatment are shown in Figure 5a and are referred as “fully hydrated”.

As one can see, the samples can be divided into two groups. H-MOR-9.9, H-MOR-15.0, H-MOR-18.7, and H-MOR-19.8, are characterized by two intense signals at about 7 ppm (L2) and 4 ppm (L3), and two signals of essentially lower intensity around 9 ppm (L1) and 1 ppm (L4). The  $^1H$  isotropic chemical shift  $\delta_{iso}$ , as well as the relative integral intensities of individual spectral lines, are listed in Table 4.

To assign lines, the samples were softly dehydrated at 100 °C in order to evacuate weakly bounded water (the procedure of dehydration is described in Section 3); the  $^1H$  MAS NMR spectra for these pre-dried samples referred as “partly dehydrated”, are shown in Figure 5b. Partial dehydration results in a redistribution of integral intensities between different components without a significant effect on  $\delta_{iso}$ . The  $^1H$  NMR spectra for MOR-15.2, H-MOR-15.7, and H-MOR-15.8 consist of one intense line at about 5.3 ppm (L3') and three lines at about 9 ppm (L1'), 7 ppm (L2') and 1 ppm (L4'). Partial dehydration, besides the redistribution between the line intensities, results in changes in chemical shifts for L1', L2', and L3' up to 1 ppm for L2' (see Table 4). Line L3 for the first group of samples and L3' for the second one can be attributed to protons of bulk water. In bulk water molecules

form an extensive network of hydrogen bonds, which results in a chemical shift of about 5.5 ppm; however, interaction with a negatively charged zeolite framework and/or cations may lead to a shift towards greater or smaller ppm [54].

**Table 4.** Isotropic chemical shifts of individual  $^1\text{H}$  MAS NMR spectral lines ( $\delta_{\text{iso}}$ ) and their relative intensities ( $I$ ) for fully hydrated and partly dehydrated samples;  $\nu_{\text{rot}} = 15$  kHz.

Sample	L1 (L1')		L2 (L2')		L3 (L3')		L4 (L4')	
	$\delta_{\text{iso}}$ (ppm)	$I$ (%)	$\delta_{\text{iso}}$ (ppm)	$I$ (%)	$\delta_{\text{iso}}$ (ppm)	$I$ (%)	$\delta_{\text{iso}}$ (ppm)	$I$ (%)
Fully hydrated								
H-MOR-9.9	9.0 ± 0.1	7.0 ± 0.1	6.8 ± 0.1	33 ± 2	4.6 ± 0.1	54 ± 2	1.3 ± 0.2	6.0 ± 0.5
H-MOR-15.0	–	–	6.8 ± 0.1	32 ± 2	4.1 ± 0.1	63 ± 2	1.2 ± 0.2	5.0 ± 0.5
H-MOR-15.2	8.9 ± 0.1	5.0 ± 0.5	6.9 ± 0.1	13 ± 1	5.3 ± 0.1	80 ± 2	1.2 ± 0.2	2.0 ± 0.5
H-MOR-15.7	8.9 ± 0.1	5.0 ± 0.5	6.6 ± 0.1	15 ± 1	5.3 ± 0.1	76 ± 2	1.2 ± 0.2	4.0 ± 0.5
H-MOR-15.8	8.8 ± 0.1	6.0 ± 0.5	6.7 ± 0.1	14 ± 1	5.3 ± 0.1	78 ± 2	1.2 ± 0.2	2.0 ± 0.5
H-MOR-18.7	8.8 ± 0.1	3.0 ± 0.5	6.8 ± 0.1	16 ± 1	4.3 ± 0.1	78 ± 2	1.3 ± 0.2	3.0 ± 0.5
H-MOR-19.8	–	–	6.8 ± 0.1	33 ± 2	4.0 ± 0.1	65 ± 2	1.3 ± 0.2	2.0 ± 0.5
Partly dehydrated								
H-MOR-9.9	9.1 ± 0.1	7.0 ± 0.1	6.8 ± 0.1	36 ± 2	4.4 ± 0.1	46 ± 2	1.7 ± 0.2	11 ± 1
H-MOR-15.0	–	–	6.9 ± 0.1	28 ± 2	4.1 ± 0.1	66 ± 2	1.3 ± 0.2	6.0 ± 0.5
H-MOR-15.2	9.1 ± 0.1	9.0 ± 0.5	7.6 ± 0.1	8 ± 1	5.4 ± 0.1	79 ± 2	1.1 ± 0.2	4.0 ± 0.5
H-MOR-15.7	9.1 ± 0.1	8.0 ± 0.5	7.6 ± 0.1	7 ± 1	5.4 ± 0.1	76 ± 2	1.1 ± 0.2	9 ± 1
H-MOR-15.8	8.6 ± 0.1	12 ± 1	6.4 ± 0.1	19 ± 1	5.4 ± 0.1	67 ± 2	1.3 ± 0.2	2.0 ± 0.5
H-MOR-18.7	8.4 ± 0.1	7.0 ± 0.5	6.7 ± 0.1	22 ± 2	4.4 ± 0.1	43 ± 2	1.8 ± 0.2	27 ± 2
H-MOR-19.8	8.7 ± 0.1	1.0 ± 0.5	6.8 ± 0.1	37 ± 2	4.0 ± 0.1	40 ± 2	1.7 ± 0.2	22 ± 2

The signal near 1 ppm (L4 and L4') is normally attributed to silanol protons not coordinated by water molecules. Extra-framework  $\text{Al}(\text{OH})_n$  complexes also contribute to this range of  $^1\text{H}$  chemical shifts. The line L2 in H-MOR-9.9, H-MOR-15.0, H-MOR-18.7, and H-MOR-19.8 corresponds to protons of  $\text{NH}_4^+$  [55] that are present in these samples, as confirmed by FTIR, see Section 2.6. Partial dehydration leads to a decrease in the ratio of integral intensities of L3/L2 lines for H-MOR-9.9, H-MOR-18.7, and H-MOR-19.8, which is most pronounced for the last two. A slight increase in the relative contribution of water molecules to the total intensity after partial dehydration in H-MOR-15.0 may indicate that, besides  $\text{NH}_4^+$ , water molecules interacting with Brønsted acid sites ( $^1\text{H}$  isotropic chemical shift at 6.4–6.5 ppm) also may contribute to L2 [39,56,57]. Unfortunately, it is not possible to separate these contributions in our experiment (applied magnetic field, rotor frequency). For the samples H-MOR-15.2, H-MOR-15.7, and H-MOR-15.8, which do not contain  $\text{NH}_4^+$  at all, see Section 2.6, the low-intensity signal L2' can be attributed to protons of  $\text{H}_2\text{O}$  molecules coordinated with Brønsted acid sites. The line L1 (L1'), which is of low intensity but is observed for all the samples except for H-MOR-15.0, can be related to free protons, which are characterized by chemical shifts of about 8–13 ppm [58–60], or  $[\text{H}_3\text{O}]^+$ , for which  $^1\text{H}$   $\delta_{\text{iso}}$  is between 7 and 9 ppm [58,61]. It should be noted that larger charged water complexes  $[\text{H} \dots (\text{H}_2\text{O})_n]^+$  may also contribute to the L2' signal [39,58].

In our previous study, we reported that, for H-MOR-15.2, an isotropic chemical shift corresponding to bulk water, as well as a signal corresponding to charged water complexes, were found to be dependent on a rotation frequency [39]. A similar effect is observed for H-MOR-15.7 and H-MOR-15.8, both hydrated and partially dehydrated, see Figure 6, whereas, for other samples,  $\delta_{\text{iso}}$  of all the individual lines is not sensitive to the rotor frequency.

It is known that under MAS conditions, despite temperature stabilization, the temperature in the rotor increases due to rotor friction with air, which could be an issue of the observed displacement of  $^1\text{H}$   $\delta_{\text{iso}}$ . However, our supplementary studies that involved temperature dependence measurements of  $^1\text{H}$  MAS NMR at low rotor frequency, and spectrum of  $^{207}\text{Pb}$  in H-MOR-15.2 mixed with  $\text{Pb}(\text{NO}_3)_2$ , confirm that the issue of such a displacement is not related to the temperature effect only [39] (the  $^{207}\text{Pb}$  chemical shift in  $\text{Pb}(\text{NO}_3)_2$  exhibits a strong temperature dependence, which makes it possible to use this compound for the temperature calibration [62]). One can suggest that in H-MOR-15.0,

H-MOR-15.7, and H-MOR-15.8 samples, prepared apparently by acid etching, this effect is caused by charge carriers. A similar effect, but much more pronounced, was reported for  $^{63}\text{Cu}$   $\delta_{\text{iso}}$  in CuI [63]. In the studied mordenite sample, such a charge carrier can be  $\text{H}^+$  or  $[\text{H}_3\text{O}]^+$ . Proton conductivity was previously discussed in a number of publications [64,65] and is consistent with the insensibility of  $^1\text{H}$   $\delta_{\text{iso}}$  to the rotor frequency for those samples of H-mordenites for which the signal associated with  $\text{H}^+$  or  $[\text{H}_3\text{O}]^+$  is absent. However, to confirm this assumption, a more thorough analysis combined with proton conductivity measurements is required.

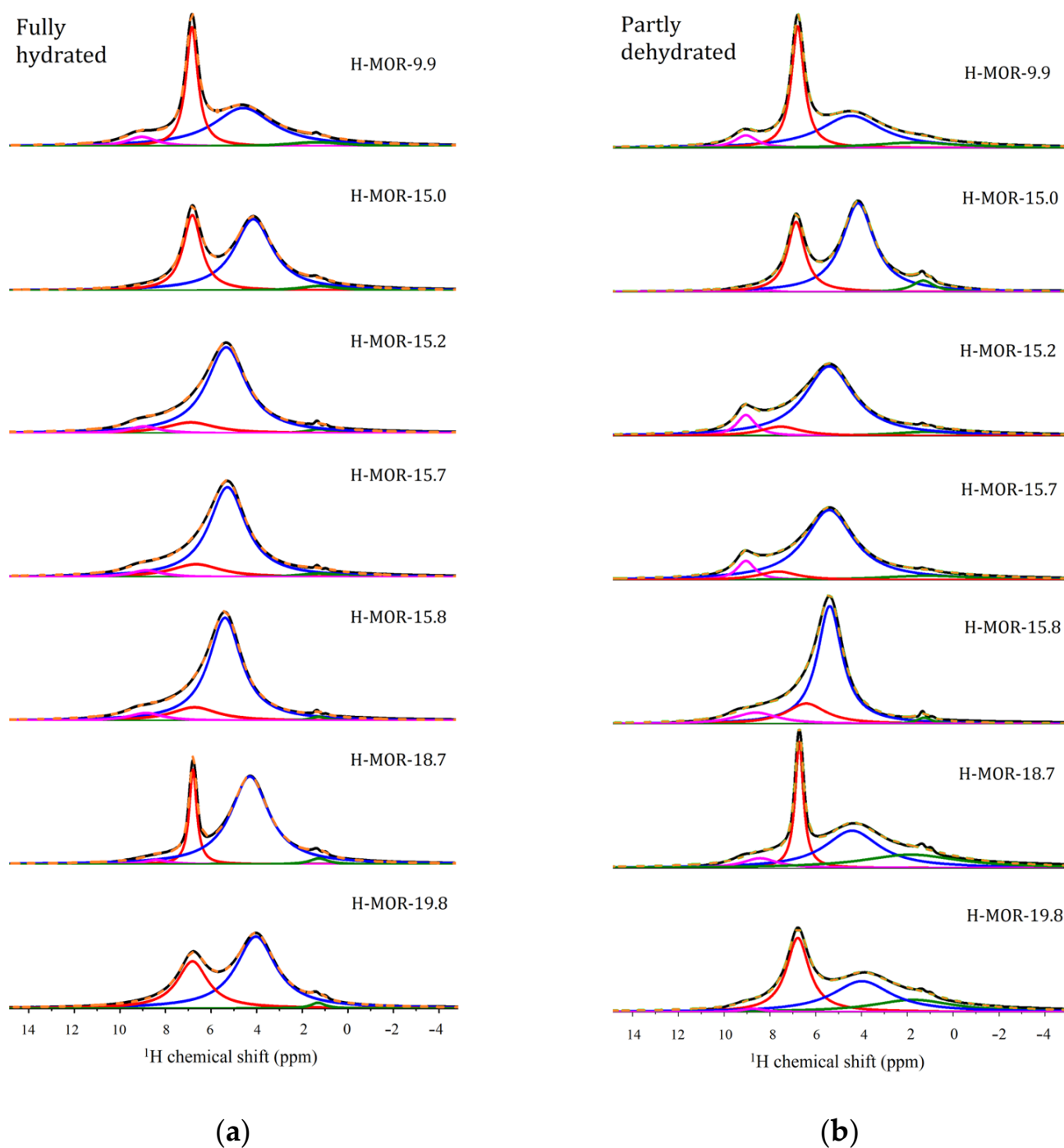


**Figure 5.**  $^1\text{H}$  MAS NMR spectra for the fully hydrated (a) and partly dehydrated (b) samples and their decomposition in Lorentzian lines. All spectra are recorded at  $\nu_{\text{rot}} = 15$  kHz.

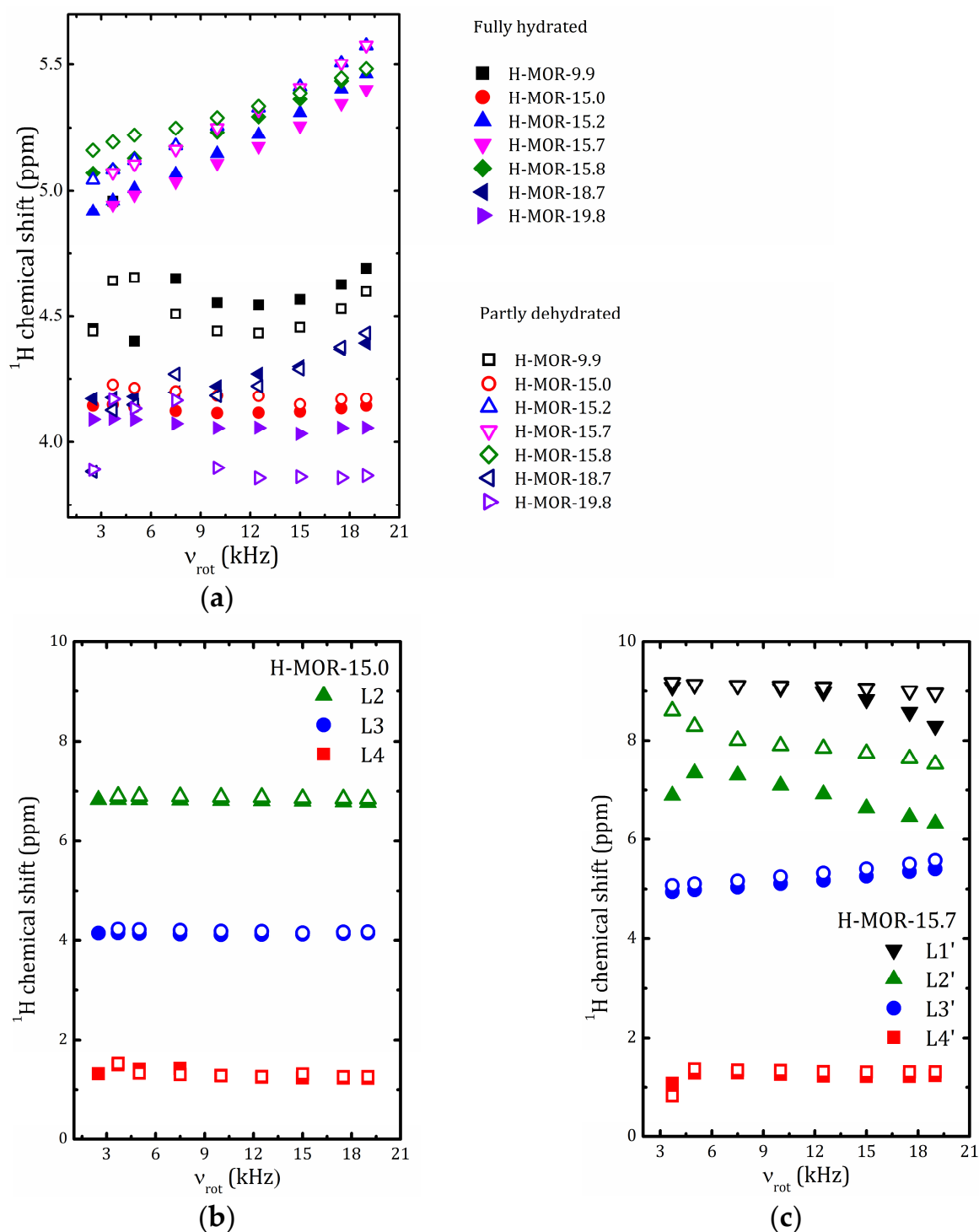


**Figure 6.**  $^1\text{H}$  NMR chemical shift of individual spectral lines at different rotor frequencies: (a)—L3 (L3') line in all the samples; (b)—L2, L3, L4 for H-MOR-15.0; (c)—L1', L2', L3' and L4' for H-MOR-15.7. Solid and open symbols correspond to the fully hydrated and partly dehydrated samples.

## 2.6. FTIR Spectroscopy Study

For FTIR studies, the samples were pressed into as thin as possible tablets (“thickness” from 9 to 18  $\text{mg}/\text{cm}^2$ ), transparent enough at 4000–1300  $\text{cm}^{-1}$  region. For thin samples, “windows” of transparency can be seen at 950–850  $\text{cm}^{-1}$  and below. The spectra of studied samples contain bands of Si-OH silanol groups at 3750–3735  $\text{cm}^{-1}$  and of Si-OH-Al zeolite bridging hydroxyls at about 3620  $\text{cm}^{-1}$ . Before thermovacuum treatment, water absorption

was always present in the spectra at 3500–3000 and about 1640–1620  $\text{cm}^{-1}$ . In the spectra of some samples, strong bands of ammonium ions were also observed at 1450–1410  $\text{cm}^{-1}$ , which in the region of stretching vibrations corresponded to a strong broad band of about 3300  $\text{cm}^{-1}$  with a “tail” from the low frequencies and a characteristic “Evans hole” at 2885  $\text{cm}^{-1}$ . The evolution of the spectrum with the increasing temperature of vacuum treatment is illustrated by the H-MOR-15.0 sample in Figure 7.

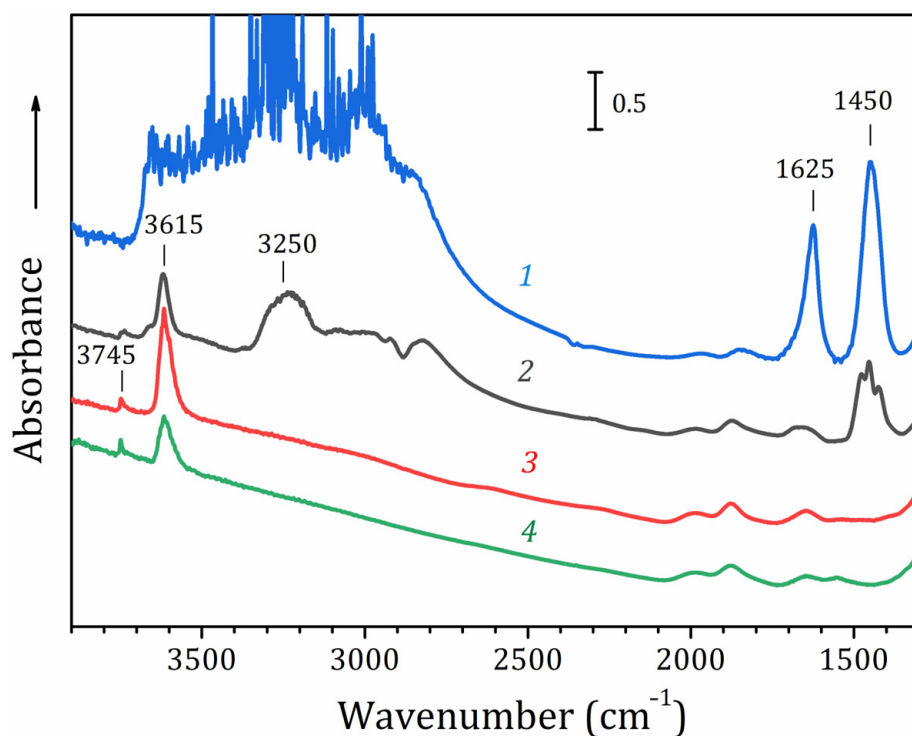


**Figure 7.** FTIR spectrum of H-MOR-15.0; 6.25  $\text{mg}/\text{cm}^2$  at ambient temperature before treatment (1) and at  $-196\text{ }^\circ\text{C}$  after evacuation at 300  $^\circ\text{C}$  (2), 450  $^\circ\text{C}$  (3) and 600  $^\circ\text{C}$  (4).

After pumping at 300  $^\circ\text{C}$  for about half an hour, the absorption of water disappears, and the ammonium bands weaken, but remain in the spectrum sometimes in the form of a group of several maxima resolved at  $-196\text{ }^\circ\text{C}$ . Heating the sample in a vacuum at 450  $^\circ\text{C}$  removes the bands of ammonium ion, while the intensity of the band of hydroxyl groups at 3615  $\text{cm}^{-1}$  significantly increases. Apparently, the new groups are formed as a result of the decomposition of ammonium ions with the liberation of ammonia. Further heating of the sample in a vacuum led to a diminishing of the OH band intensity, while no other changes occur in the spectrum.

The samples were usually evacuated at 300 and 450  $^\circ\text{C}$ , sometimes at higher temperatures, then adsorption of CO was studied at the temperature of liquid nitrogen ( $-196\text{ }^\circ\text{C}$ ) after preliminary registering the spectrum of the cooled sample in the presence of about 0.5 torr of helium for better thermal contact with the cold walls of the cell. Usually, a significant amount of adsorbate was first introduced, until the sample was saturated when the CO pressure was 2–5 torr. Then, CO was removed by pumping for a different time, always adding helium. If the bands remained too intense, the sample was vacuumed in a warmer part of the cell. The spectra of CO adsorbed on H-MOR-15.0 after different pretreatment conditions are shown in Figure 8. One can see the increase in the 2178  $\text{cm}^{-1}$  band intensity after pretreatment at 450  $^\circ\text{C}$  when new OH groups are formed as a result of ammonium decomposition. Diminishing of this band after sample evacuation at 600  $^\circ\text{C}$  is accompanied by the appearance of a band at 2225  $\text{cm}^{-1}$ . We can also point to the decreased intensity of the band at 2156  $\text{cm}^{-1}$  after treatment at 450  $^\circ\text{C}$ .

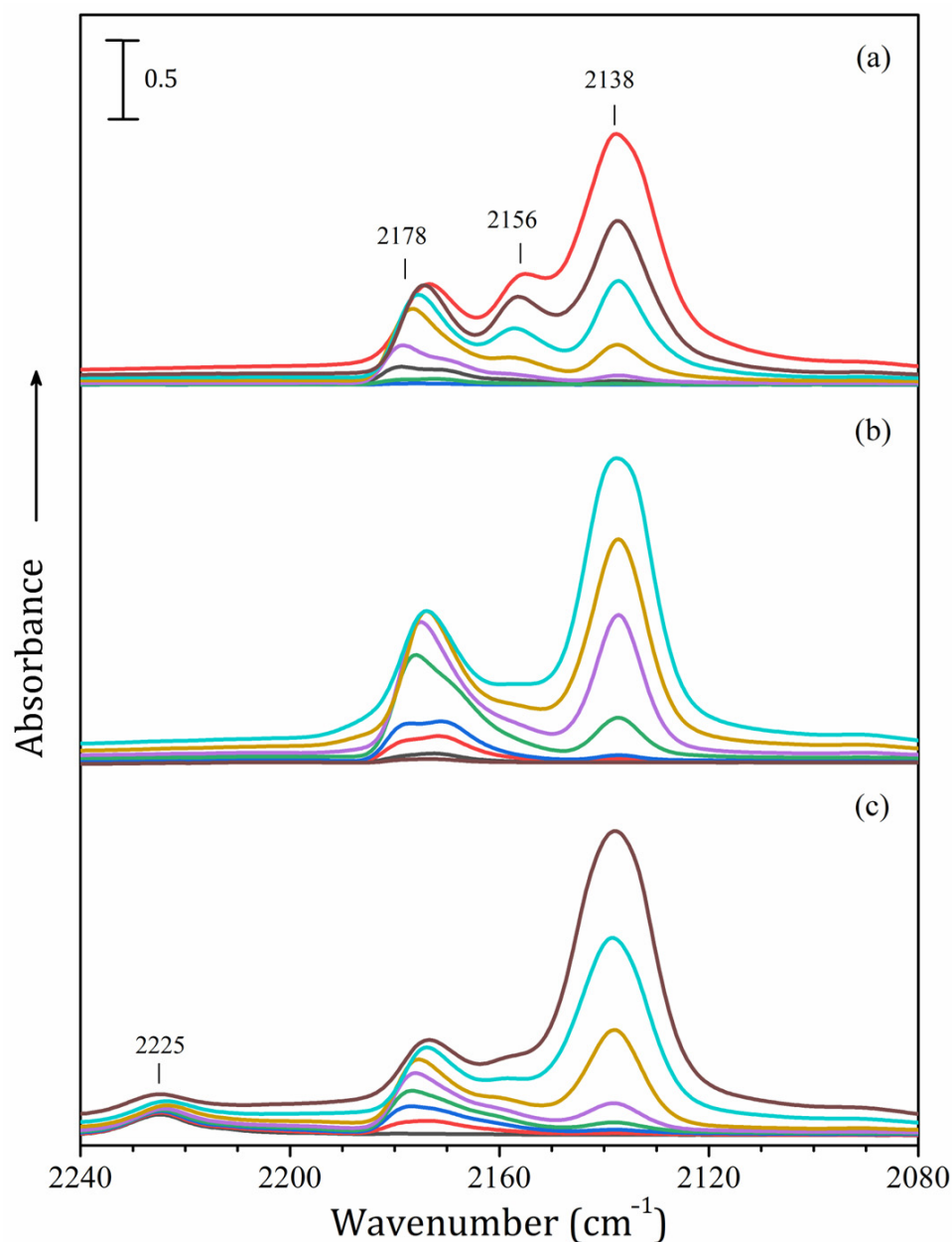


**Figure 8.** Evolution of FTIR spectra of CO adsorbed on HMOR-15.0 pretreated at 300 °C (a), 450 °C (b), and 600 °C (c), in course of desorption. Spectra are registered at  $-196$  °C in the presence of *ca* 0.5 torr of helium.

Analysis of these data enables us to distinguish up to five absorption bands in the spectra of adsorbed CO. Under saturation conditions, there is always a band of “physically adsorbed” molecules at  $2138\text{ cm}^{-1}$ , which decreases rapidly in intensity as pumping proceeds. The intensity of the band at  $2160\text{--}2155\text{ cm}^{-1}$  correlates with the perturbation of the band of silanol groups, which, under the action of adsorbed CO, shifts to about  $3640\text{ cm}^{-1}$  (Figure 9, curve 2) Pumping at nitrogen temperature quickly leads to the disappearance of this form of adsorption. The most stable form of adsorbed CO manifests itself as a relatively weak band at  $2225\text{ cm}^{-1}$ , which disappears only after sufficiently long pumping at room temperature. This band is especially intense after treatment at high temperatures. For some samples, it is accompanied by bands at  $2205\text{--}2199\text{ cm}^{-1}$  (H-MOR-19.8 and H-MOR-18.7 treated at 450 °C).

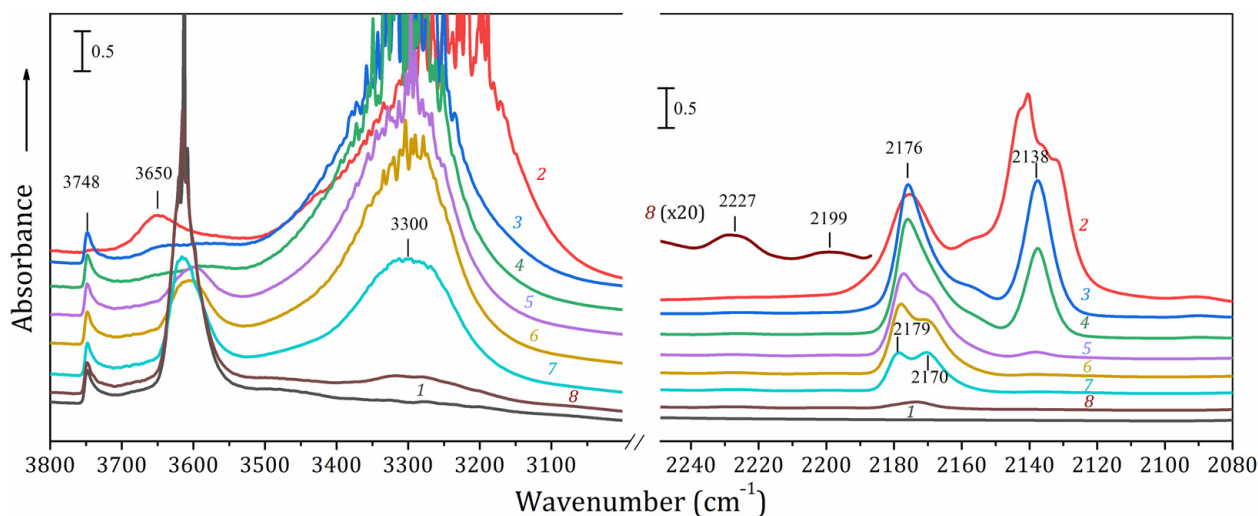


**Figure 9.** FTIR spectrum of CO adsorbed on H-MOR-19.8 pretreated at 450 °C before (1) and after adsorption of CO (2), and on gradual desorption (3–8). Spectra are registered at  $-196$  °C in the presence of *ca* 0.5 torr of helium.

The bridged hydroxyls Si-OH-Al, which account for Brønsted acidity of zeolites, absorb at  $3620\text{--}3610\text{ cm}^{-1}$ . Their perturbation by CO results in the vanishing of this band and the appearance of a broad band of perturbed OH groups with a maximum of about  $3300\text{ cm}^{-1}$ . At saturating coverages, the maximum of this band shifts towards low frequencies up to  $3250\text{ cm}^{-1}$  or even slightly lower (curve 2 in Figure 9). In the spectrum of CO, this form of adsorption corresponds to a band that appears at  $2175\text{--}2165\text{ cm}^{-1}$  and with the decrease in coverage slightly shifts towards high frequencies to  $2178\text{ cm}^{-1}$ . With further desorption of CO, it turns out to consist of two poorly resolved maxima, of which not the highest frequency, but the underlying one remains before the disappearance at  $2075\text{--}2073\text{ cm}^{-1}$ . The corresponding band of perturbed hydroxyls is still visible at  $3300\text{ cm}^{-1}$ . In the difference spectra, one can see that the additional disturbance of hydroxyls with a shift up to  $3250\text{ cm}^{-1}$  correlates with the growth of the band at  $2138\text{ cm}^{-1}$ .

Spectra obtained reveal different kinds of surface sites. There are two types of surface hydroxyl groups, silanols and zeolitic, and both act as the centers of CO adsorption. In addition, CO interacts with framework surface oxygen atoms forming side-on complexes [66] characterized by the band at  $2138\text{ cm}^{-1}$ . The band at  $2225\text{ cm}^{-1}$  should be assigned to molecules coordinately bound to strong Lewis sites, apparently,  $\text{Al}^{3+}$  ions in an uncomplete tetrahedral coordination [67,68]. The intensity of this band grows after treating the sample at  $600$  °C when decreasing the intensity of bridging hydroxyls testifies for their desorption. This means that it can be framework aluminum, which becomes accessible for CO after the removal of the bridged OH group on the formation of the water molecule with a proton of neighboring hydroxyl. However, in the spectra of some samples the band at this or close position is present already after pretreatment at  $450$  °C (sample H-MOR-18.7) or even at  $300$  °C (sample H-MOR-15.7). We suppose that in this case, it belongs to extra-framework  $\text{Al}^{3+}$  ions. For the H-MOR-18.7 sample treated at  $450$  °C, one more band can also be seen at  $2206\text{ cm}^{-1}$  (sample H-MOR-18.7 Figure 9, curve 8). As soon as there are no other cations in this sample, it could be also assigned to extra-framework  $\text{Al}^{3+}$  ions in somewhat different coordination, typical of alumina surface [67].

Intensities of the bands of CO adsorbed on zeolitic OH groups follow the concentration of the latter. For H-MOR-15.0 pretreated at  $300$ ,  $450$ , and  $600$  °C the total integrated intensity at  $2180\text{--}2165\text{ cm}^{-1}$  first increases when the number of OH groups grows as a result of ammonium decomposition and lowers on further heating the sample at  $600$  °C with the decrease in the OH band intensity. However, the CO band at about  $2156\text{ cm}^{-1}$  assignable to molecules adsorbed on silanol groups is the most intense after pumping at  $300$  °C (Figure 8a), while the intensity of silanol groups, on the contrary, grows by about 60%

after heating at 450 °C and even a little bit more on treatment at 600 °C when the intensity of corresponding CO band also slightly increases. To our mind, the extra intensity of the 2156  $\text{cm}^{-1}$  band in the spectra of samples treated at 300 °C is due to CO interacting with ammonium ions. Strong absorption of perturbed OH groups prevents observation of stretching N-H modes, but small changes in the band shape of the  $\text{NH}_4^+$  bending vibration band are consistent with this explanation.

Figure 10 shows the spectra of CO adsorbed on the H-MOR-18.7 sample pretreated at 300 °C and registered at  $-196$  °C for three successively different coverages and the results of their deconvolution. As one can see, the maxima of the components in the deconvoluted spectrum do not differ much and remain at about 2178, 2170, 2160, and 2138  $\text{cm}^{-1}$ , while the relative intensities seriously change.

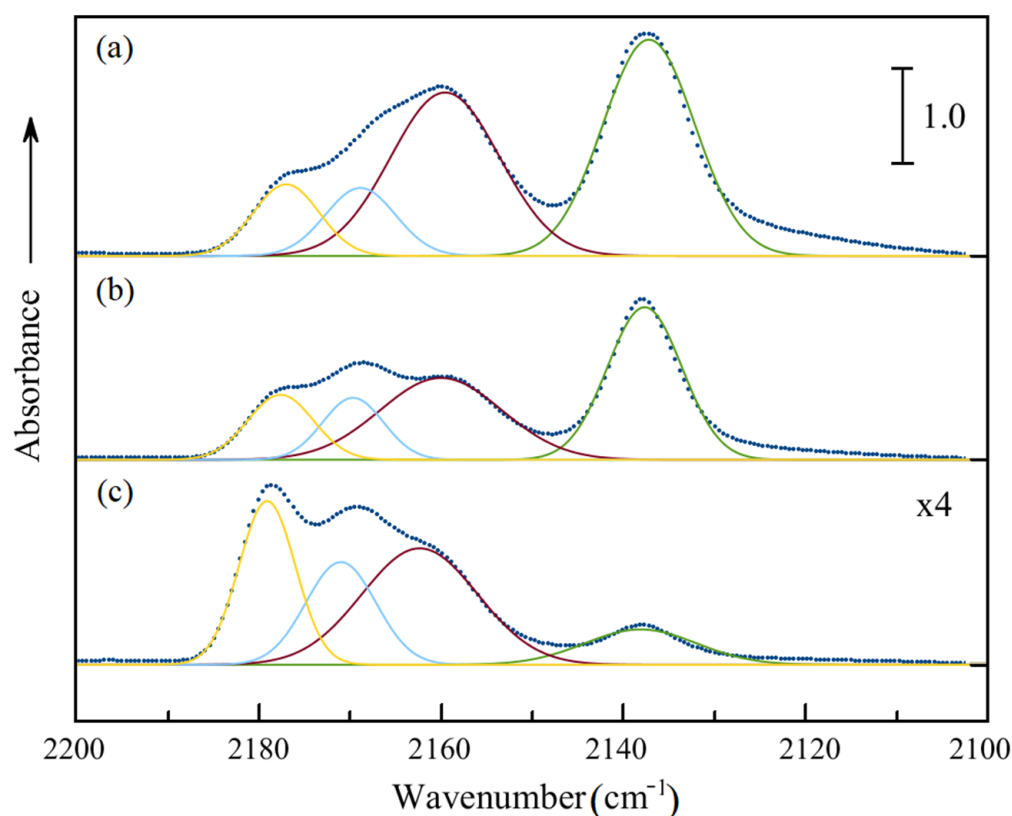


**Figure 10.** FTIR spectrum of CO adsorbed on HMOR-18.7 pretreated at 300 °C registered at  $-196$  °C for three successively diminishing coverages (a–c) and the results of their deconvolution (the parameters of the spectra deconvolution are given in the Supplementary Materials, Table S2). Approximate positions of the four maxima are 2178, 2170, 2160, and 2138  $\text{cm}^{-1}$ .

Obtained in this way, intensities of the bands related to the thickness of samples in  $\text{mg}/\text{cm}^2$  for CO adsorbed on different sites of the studied samples are presented in Table 5. From these figures, using the known values of integrated extinction coefficient  $\epsilon$  we can easily estimate the concentration of corresponding surface sites. There are some contradictions about the values of  $\epsilon$  for adsorbed CO [69,70]. Here, we use values from [69], where it was measured for molecules adsorbed on silanol groups of aerosil ( $\epsilon = 1.6 \text{ cm}/\mu\text{mol}$ ) and on hydroxyls of HZSM-5 zeolite ( $\epsilon = 2.1 \text{ cm}/\mu\text{mol}$ ). For CO adsorbed on aluminum cations we take a value of  $\epsilon = 0.2 \text{ cm}/\mu\text{mol}$ , obtained for strong Lewis sites of  $\text{TiO}_2$ , for which the frequency of adsorbed molecules ( $2210 \text{ cm}^{-1}$ ) is the nearest to that of CO interacting with  $\text{Al}^{3+}$  in our case ( $2225\text{--}2206 \text{ cm}^{-1}$ ). Here, we give in the table for H-MOR-18.7 the sum of intensities of two bands at these wavenumbers. Recently, the integrated extinction coefficient  $\epsilon$  was determined for the stretching OH bands of silanols and bridged Si-OH-Al groups of H-ZSM-5 and H-ZSM-23 zeolites from the comparison of band intensities in the

IR spectra with the concentration of corresponding protons measured by  $^1\text{H}$  MAS NMR spectra of the same samples [71]. These data enable us to estimate the concentration of silanol and bridged OH groups directly from the band intensities in the OH vibration region of the same spectra. Spectra presented in Figures 8–10 reveal a structure of the band at  $2180\text{--}2160\text{ cm}^{-1}$ , which consists of at least two bands. This is in agreement with the data reported in [72,73] that there are two or even three kinds of bridged OH groups in mordenite, differing in their location in the framework of zeolite. Analysis of mordenite structure shows that there are ten crystallographically distinct oxygen atoms and hence, there could be ten different acidic hydroxyls, at least six of which were visualized by distinct bands in the deconvoluted FTIR spectra [34]. In the corresponding column of Table 5 we show the total intensity of bands in this spectral region.

**Table 5.** Band intensities of adsorbed CO  $I_{\text{CO}}$  and hydroxyl groups  $I_{\text{OH}}$ , type and concentration  $N$  of active sites according to FTIR spectra, extinction coefficient values  $\epsilon$  used to estimate  $N$  and quantity of Al atoms for the samples pretreated at  $450\text{ }^\circ\text{C}$ .

Type of Sites	Lewis Acid Sites		Brønsted Acid Sites			Al Content	Silanol Hydroxyls		
$\nu$ ( $\text{cm}^{-1}$ )	2230–2200		2180–2170		3620		3747		
$\epsilon$ ( $\text{cm}/\mu\text{mol}$ )	$0.2^1$		$2.1^1$		$3.06^2$		$1.5^2$		
Sample	$I_{\text{CO}}$ ( $\text{cm}/\text{mg}$ )	$N_{\text{L}}$ ( $\mu\text{mol}/\text{g}$ )	$I_{\text{CO}}$ ( $\text{cm}/\text{mg}$ )	$N_{\text{B}}$ ( $\mu\text{mol}/\text{g}$ )	$I_{\text{OH}}$ ( $\text{cm}/\text{mg}$ )	$N_{\text{B}}$ ( $\mu\text{mol}/\text{g}$ )	$N_{\text{Al}}$ ( $\mu\text{mol}/\text{g}$ )	$I_{\text{OH}}$ ( $\text{cm}/\text{mg}$ )	$N_{\text{S}}$ ( $\mu\text{mol}/\text{g}$ )
H-MOR-9.9	$0.017 \pm 0.002^4$	$85 \pm 9$	$2.3 \pm 0.1$	$1100 \pm 60$	$9.4 \pm 0.2$	$3100 \pm 500$	$2860 \pm 30$	$0.44 \pm 0.09$	$300 \pm 60$
H-MOR-15.0	$0.008 \pm 0.001$	$40 \pm 6$	$2.1 \pm 0.1$	$1000 \pm 50$	$7.0 \pm 0.1$	$2300 \pm 100$	$2070 \pm 20$	$0.19 \pm 0.04$	$120 \pm 20$
H-MOR-15.2	$0.07 \pm 0.01$	$350 \pm 40$	$1.9 \pm 0.1$	$900 \pm 50$	off scale		$1670 \pm 20$	$2.0 \pm 0.8$	$1300 \pm 500$
H-MOR-15.7	$0.087 \pm 0.009$	$430 \pm 40$	off scale		off scale		$1660 \pm 20$	$1.5 \pm 0.8$	$1000 \pm 600$
H-MOR-15.8	$0.085 \pm 0.008$	$420 \pm 40$	$2.4 \pm 0.1$	$1140 \pm 60$	$6.7 \pm 0.9$	$2200 \pm 300$	$1660 \pm 20$	$2.1 \pm 0.3$	$1460 \pm 200$
H-MOR-18.7	$0.027 \pm 0.004^3$	$130 \pm 20$	$2.3 \pm 0.1$	$1100 \pm 60$	$3.7 \pm 0.6$	$1200 \pm 200$	$1640 \pm 20$	$0.28 \pm 0.04$	$190 \pm 30$
H-MOR-19.8	$0.014 \pm 0.003$	$70 \pm 20$	$2.4 \pm 0.1$	$1140 \pm 60$	$8.3 \pm 0.7$	$2700 \pm 200$	$1660 \pm 20$	$0.32 \pm 0.05$	$210 \pm 30$

<sup>1</sup> From Reference [69]. <sup>2</sup> From Reference [71]. <sup>3</sup> The concentration of Lewis acid sites is determined from the integral intensity in the  $\nu$  range of  $2240\text{--}2190\text{ cm}^{-1}$ . <sup>4</sup> The estimated experimental error values correspond to spectral measurements and do not include the uncertainty of  $\epsilon$  values. The listed values can be, thus taken into account for comparison of different samples, but systematic errors are not excluded when comparing the data for different sites or obtained by different methods.

The concentration of Lewis  $\text{Al}^{3+}$  sites, zeolitic bridged OH groups (Brønsted centers), and silanol hydroxyls, obtained from the intensities of corresponding bands in the studied spectra, are denoted in Table 5 as  $N_{\text{L}}$ ,  $N_{\text{B}}$ , and  $N_{\text{S}}$ , respectively. The latter values were calculated both from the intensities of the bands of adsorbed CO at about  $2156\text{ cm}^{-1}$  in the deconvoluted spectra registered at saturating conditions and from the intensities of the band of silanol groups at about  $3747\text{ cm}^{-1}$ , using  $\epsilon$  values from [69] or [71], respectively. For H-MOR-15.2 and H-MOR-15.8 samples, where silanol concentration is comparatively high and the band of CO bound to them is well resolved, the values obtained by the two ways coincide within the error of measurements. For other samples the CO band was too weak, hidden between strong bands of other forms of adsorption, and could not be measured correctly. That is why for the silanols we present in the table the data obtained from the OH band intensities.

The concentration of bridged hydroxyls was also estimated spectroscopically either from OH band intensity or from the bands of adsorbed CO. Unfortunately, not all our samples were transparent enough in the OH stretching region, and for some samples, CO intensities were too strong at high coverages. Data presented in the table correspond to the stage when the excess of CO was removed by pumping for several minutes, the band at  $2138\text{ cm}^{-1}$  started to diminish and the band of unperturbed OH groups at  $3620\text{ cm}^{-1}$  did not start to recover. One could anticipate that the  $N_{\text{B}}$  value would correlate with the concentration of aluminum in the framework decreasing with the growing  $\text{SiO}_2/\text{Al}_2\text{O}_3$  ratio. The corresponding values were calculated based on the  $\text{SiO}_2/\text{Al}_2\text{O}_3$  ratios obtained by NMR ( $^{27}\text{Al}$ )<sup>1</sup> spectra given in Table 1. As anticipated, the highest amount of Brønsted

acid sites, found from the OH band intensities, was for the H-MOR-9.9 sample, however, for H-MOR-19.8 it happened to be unexpectedly great. It should be noted that for all the studied samples, except H-MOR-18.7, the obtained values are noticeably greater than the concentration of framework aluminum, although these values should be close to each other. It is well possible that the  $\epsilon$  value for OH groups for mordenite is not the same as measured in [71].

Values of Brønsted site concentrations found from CO band intensities, on the contrary, appeared to be lower than that of the amount of framework aluminum atoms and almost constant for all the studied samples. To some extent, this also could be due to  $\epsilon$  value of adsorbed CO, which as well was measured for other zeolites, but this does not explain the resemblance of the Brønsted site amount for different samples. We suppose that the bands in the 2180–2170  $\text{cm}^{-1}$  region are due to molecules adsorbed on the most accessible sites of the main channel, while those confined in the side pockets of mordenite structure are not able to form the same H-bond and absorb at lower wavenumbers overlapping with the bands of molecules adsorbed on weaker sites.

The number of Lewis sites  $N_L$  measured from the intensity of the CO band at 2225  $\text{cm}^{-1}$  correlates well with the data on extra-framework aluminum concentration shown in Figure 4. It is comparatively high for H-MOR-15.7, H-MOR-15.8, and H-MOR-18.7, moderate for H-MOR-9.9 and H-MOR-19.8, and negligible for H-MOR-15.0. We can hardly expect the quantitative correlation between the number of extra-framework aluminum atoms and that of CO molecules which account for the 2225  $\text{cm}^{-1}$  band because it is not clear if every such atom can strongly coordinate CO. Moreover, the  $\epsilon$  value for CO was estimated only tentatively. Nevertheless, the obtained spectroscopically number  $N_L$  for such sites for H-MOR-15.2, H-MOR-15.7, and H-MOR-15.8 samples is 20–26% of the amount of framework aluminum. This is in fair agreement with the intensity ratio of bands in the NMR  $^{27}\text{Al}$  spectra shown in Figure 4 and presented in Table 3.

### 3. Materials and Methods

A set of samples of protonated mordenites with nominal  $\text{SiO}_2/\text{Al}_2\text{O}_3$  molar ratios of 9.9, 15.0, 15.2, 15.7, 15.8, 18.7, and 19.8, respectively, was studied. Samples were provided by TOSOH Co., Tokyo, Japan, however, the details of their synthesis constitute the “know-how” of the company.

XRD studies were carried out using the Bruker “D8 DISCOVER” (Bruker AXS, Karlsruhe, Germany) research complex with Cu-K $\alpha$  radiation (scan range: from 5.0017 to 69.9953 2-theta degree, step width: 0.0202 degrees). Quantification was performed using the DIFFRAC.SUITE software package.

The morphology of the samples was studied by a Zeiss Libra 200FE (Carl Zeiss AG, Oberkochen, Germany) scanning electron microscope. EDX measurements were carried out applying Analytical Silicon Drift Detector: X-Max (Oxford Instruments Inc., Abingdon, UK). The bulk elemental compositions were determined ICP-OES using Shimadzu ICPE-9000 (Shimadzu Corporation, Kyoto, Japan). XPS measurements were completed by using a Combined Auger, X-ray, and Ultraviolet Photoelectron spectrometer Thermo Fisher Scientific ESCALab 250Xi (Thermo Fisher Scientific, Waltham, MA, USA) with AlK $\alpha$  radiation (photon energy 1486.6 eV) with total energy resolution of 0.3 eV.

TG analysis was performed using a Netzsch TG 209 F1 Libra (Netzsch-Gruppe, Selb, Germany) in the temperature range from 40 to 750 °C at the heating rate of 10 °C/min in argon stream at the rate of 30 mL/min.

For IR studies, a powdered sample was pressed into thin tablets (depending on the sample and experiment, the thickness was varied from 9 to 18  $\text{mg}/\text{cm}^2$ ). A rectangle was then cut out of the disk to fit into a homemade sample holder. The sample was inserted into a low-temperature IR cell (its description can be found in Ref. [74]). Samples were preheated in vacuum (residual pressure  $< 10^{-4}$  torr) for 40 min inside the IR cell, activation temperatures 300, 450, and 600 °C. The spectra were recorded using a Nicolet 710 IR

Fourier transform spectrometer (Madison, WI, USA) with a coolable MCT detector, with a resolution of  $2\text{ cm}^{-1}$ . For each spectrum, 128 scans were used.

NMR studies were carried out using a Bruker Avance IIIWB 400 MHz solid-state NMR spectrometer (Bruker Corporation, Billerica, MA, USA) operating with Topspin version 3.2 and using a CP-MAS 3.2 mm probe. The studies were carried out at room temperature. The operating frequencies were 400.23, 104.28, and 79.5 MHz for  $^1\text{H}$ ,  $^{27}\text{Al}$ , and  $^{29}\text{Si}$  nuclei, respectively.  $^{27}\text{Al}$  and  $^{29}\text{Si}$  MAS NMR spectra were acquired at a rotor speed of 15 kHz.  $^1\text{H}$  NMR spectra were recorded at the rotor speed varied from 2.5 to 19 kHz. Proton spectra were recorded for fully hydrated samples, and for mildly dehydrated samples, the samples were pre-dried for 4 h at a temperature of  $100\text{ }^\circ\text{C}$  in a desiccator and sealed into ampoules. Chemical shifts were determined against/relative to  $\text{AlCl}_3$  solution and TMS as external standards.

Spectra deconvolution was completed using MagicPlot Pro software [75].

#### 4. Conclusions

A set of H-mordenite catalysts with a nominal MR varied ranging from 9.9 to 19.8 was studied by various methods, including XRD, XPS, SEM-EDX, ICP-OES, TGA, MAS NMR, and FTIR.

The samples exhibit different morphologies and inhomogeneity of element distribution from the surface to the depth of the crystal. XRD analysis confirms that all samples retain the mordenite crystalline structure. The ellipticity of the main mordenite channel varies as MR changes, which may be a consequence of different arrangements of Al tetrahedra, and, accordingly, compensating cations and/or Brønsted acid sites in the zeolite structure. Samples, that do not contain  $\text{NH}_4^+$  cations (H-MOR-15.2, H-MOR-15.7, H-MOR-15.8) and presumably prepared by acid etching, exhibit the strongest compression of the main channel.

$^{27}\text{Al}$  MAS NMR provides evidence for the presence of extra-framework Al in most samples that results in higher real MR as compared to the nominal values.  $^{29}\text{Si}$  MAS NMR spectra suggest the presence of Q3(0Al) sites in H-MOR-15.2, H-MOR-15.7, and H-MOR-15.8 that correlate with the amount of silanol groups estimated by FTIR.

$^1\text{H}$  MAS NMR of fully hydrated and partly dehydrated samples confirms presence of  $\text{NH}_4^+$  cations in all the samples except H-MOR-15.2, H-MOR-15.7, and H-MOR-15.8 (that is also supported by FTIR), free bulk water, water interacting with Brønsted acid sites, silanol protons not bound to water molecules and  $\text{H}^+$  or  $[\text{H}_3\text{O}]^+$  cations (a signal at about 9 ppm) For H-MOR-15.2, H-MOR-15.7, and H-MOR-15.8 a dependence of  $^1\text{H}$  isotropic chemical shift of the signals attributed to water on the rotor frequency was found. The effect is not very pronounced but not negligible and is presumably due to the movement of charge carriers.

FTIR studies of CO absorbed at  $-196\text{ }^\circ\text{C}$  on H-mordenite samples enables us to estimate the concentration of different active sites: Lewis acid sites, Brønsted acid sites and silanol hydroxyls. The concentration of Lewis acid sites as determined from FTIR is in fair agreement with  $^{27}\text{Al}$  MAS NMR data. However, the quantity of Brønsted acid sites is essentially constant for all the studied samples and does not correlate directly with MR determined from  $^{29}\text{Si}$  MAS NMR. Alternatively, the concentration of Brønsted hydroxyls and silanol groups was obtained from their band intensities in the OH stretching vibration region using the published values of the integrated absorption coefficients. The spectroscopically measured concentration values are compared with the amount of framework aluminum atoms calculated from MR values based on  $^{27}\text{Al}$  MAS NMR measurements. The comparison shows that the number of Brønsted sites obtained from OH band intensities is slightly overestimated, while that one measured from the CO band intensities, on the contrary, is lower than the expected value. The discrepancy can be presumably explained by steric hindrances preventing H-bond formation for molecules confined in the side pockets of the mordenite lattice. The estimated values of Lewis site concentration

quantitatively correlate with the amount of extra-framework aluminum from  $^{27}\text{Al}$  MAS NMR measurements.

**Supplementary Materials:** The following supporting information can be downloaded at: <https://www.mdpi.com/article/10.3390/catal13020344/s1>, Table S1: Elemental composition in  $\text{mg}/\text{dm}^3$  of the studied samples determined by ICP-OES. Table S2: Parameters of the Gaussian lines for the FTIR spectra deconvolution in Figure 10: frequency ( $\nu$ ), half width at half maximum (HWHM), and area under the curve ( $\sigma$ ).

**Author Contributions:** Conceptualization, M.G.S., A.A.T. and V.P.; methodology, M.G.S., A.S.M., A.A.T. and V.P.; validation, M.G.S. and A.A.T.; formal analysis, M.G.S. and A.A.T.; investigation, E.A.K., A.S.M., Y.V.S. and E.A.S.; writing—original draft preparation, M.G.S. and A.A.T.; writing—review and editing, M.G.S., A.A.T. and V.P.; visualization, M.G.S., E.A.K., Y.V.S. and E.A.S.; supervision, M.G.S., project administration, M.G.S.; funding acquisition, M.G.S. All authors have read and agreed to the published version of the manuscript.

**Funding:** This study was supported by the Russian Science Foundation within the framework of project No. 23-23-00448.

**Data Availability Statement:** Data sharing is not applicable to this article.

**Acknowledgments:** The studies were carried out at the Research Park of Saint Petersburg State University: Centre for Physical Methods of Surface Investigation, Centre of Thermal Analysis and Calorimetry, Centre for X-ray Diffraction Studies, Centre for Magnetic Resonance, Chemical Analysis and Materials Research Centre, Interdisciplinary Resource Centre for Nanotechnology.

**Conflicts of Interest:** The authors declare no conflict of interest.

## References

1. Breck, D.W. *Zeolite Molecular Sieves: Structure, Chemistry, and Use*; John Wiley and Sons: New York, NY, USA; London, UK; Sydney, Australia; Toronto, ON, Canada, 1974; ISBN 0471099856.
2. Baerlocher, C.; McCusker, L.B. Database of Zeolite Structures. Available online: <http://www.iza-structure.org/databases/> (accessed on 11 November 2022).
3. Van Speybroeck, V.; Hemelsoet, K.; Joos, L.; Waroquier, M.; Bell, R.G.; Catlow, C.R.A. Advances in theory and their application within the field of zeolite chemistry. *Chem. Soc. Rev.* **2015**, *44*, 7044–7111. [[CrossRef](#)]
4. Rodríguez-Iznaga, I.; Shelyapina, M.G.; Petranovskii, V. Ion Exchange in Natural Clinoptilolite: Aspects Related to Its Structure and Applications. *Minerals* **2022**, *12*, 1628. [[CrossRef](#)]
5. Sun, Q.; Wang, N.; Yu, J. Advances in Catalytic Applications of Zeolite-Supported Metal Catalysts. *Adv. Mater.* **2021**, *33*, 2104442. [[CrossRef](#)]
6. Sánchez-López, P.; Kotolevich, Y.; Yocupicio-Gaxiola, R.I.; Antúnez-García, J.; Chowdari, R.K.; Petranovskii, V.; Fuentes-Moyado, S. Recent Advances in Catalysis Based on Transition Metals Supported on Zeolites. *Front. Chem.* **2021**, *9*, 1–25. [[CrossRef](#)] [[PubMed](#)]
7. Tahraoui, Z.; Nouali, H.; Marichal, C.; Forler, P.; Klein, J.; Daou, T.J. Influence of the Compensating Cation Nature on the Water Adsorption Properties of Zeolites. *Molecules* **2020**, *25*, 944. [[CrossRef](#)] [[PubMed](#)]
8. Antúnez-García, J.; Galván, D.; Petranovskii, V.; Murrieta-Rico, F.N.; Yocupicio-Gaxiola, R.I.; Shelyapina, M.G.; Fuentes-Moyado, S. The effect of chemical composition on the properties of LTA zeolite: A theoretical study. *Comput. Mater. Sci.* **2021**, *196*, 110557. [[CrossRef](#)]
9. Valtchev, V.; Majano, G.; Mintova, S.; Pérez-Ramírez, J. Tailored crystalline microporous materials by post-synthesis modification. *Chem. Soc. Rev.* **2012**, *42*, 263–290. [[CrossRef](#)] [[PubMed](#)]
10. Wheatley, P.S.; Chlubná-Eliášová, P.; Greer, H.; Zhou, W.; Seymour, V.R.; Dawson, D.M.; Ashbrook, S.E.; Pinar, A.B.; McCusker, L.B.; Opanasenko, M.; et al. Zeolites with Continuously Tuneable Porosity. *Angew. Chem. Int. Ed.* **2014**, *53*, 13210–13214. [[CrossRef](#)]
11. Zvereva, I.A.; Shelyapina, M.G.; Chislov, M.; Novakowski, V.; Malygina, E.; Rodríguez-Iznaga, I.; Hernández, M.-A.; Petranovskii, V. A comparative analysis of natural zeolites from various Cuban and Mexican deposits: Structure, composition, thermal properties and hierarchical porosity. *J. Therm. Anal. Calorim.* **2021**, *147*, 6147–6159. [[CrossRef](#)]
12. Barthomeuf, D. Zeolite acidity dependence on structure and chemical environment. Correlations with catalysis. *Mater. Chem. Phys.* **1987**, *17*, 49–71. [[CrossRef](#)]
13. Mihályi, R.; Lázár, K.; Kollár, M.; Lónyi, F.; Pál-Borbély, G.; Szegedi, Á. Structure, acidity and redox properties of MCM-22 ferrisilicate. *Microporous Mesoporous Mater.* **2008**, *110*, 51–63. [[CrossRef](#)]
14. Catizzzone, E.; Migliori, M.; Mineva, T.; van Daele, S.; Valtchev, V.; Giordano, G. New synthesis routes and catalytic applications of ferrierite crystals. Part 2: The effect of OSDA type on zeolite properties and catalysis. *Microporous Mesoporous Mater.* **2020**, *296*, 109988. [[CrossRef](#)]

15. Derbe, T.; Temesgen, S.; Bitew, M. A Short Review on Synthesis, Characterization, and Applications of Zeolites. *Adv. Mater. Sci. Eng.* **2021**, *2021*, 6637898. [[CrossRef](#)]
16. Xu, H.; Wu, P. New progress in zeolite synthesis and catalysis. *Natl. Sci. Rev.* **2022**, *9*, nwac045. [[CrossRef](#)]
17. Sharma, V.; Javed, B.; Byrne, H.; Curtin, J.; Tian, F. Zeolites as Carriers of Nano-Fertilizers: From Structures and Principles to Prospects and Challenges. *Appl. Nano* **2022**, *3*, 163–186. [[CrossRef](#)]
18. Ivankovic, T.; Dikic, J.; du Roscoat, S.R.; Dekic, S.; Hrenovic, J.; Ganjto, M. Removal of emerging pathogenic bacteria using metal-exchanged natural zeolite bead filter. *Water Sci. Technol.* **2019**, *80*, 1085–1098. [[CrossRef](#)]
19. Nizam, M.K.; Azhari, S.; Jaya, M.A.T. Modified Zeolite as Purification Material in Wastewater Treatment: A Review. *Sci. Res. J.* **2021**, *18*, 177–213. [[CrossRef](#)]
20. Vogt, E.T.; Whiting, G.T.; Chowdhury, A.D.; Weckhuysen, B.M. Zeolites and Zeotypes for Oil and Gas Conversion. In *Advances in Catalysis*; Academic Press: Cambridge, MA, USA, 2015; Volume 58, pp. 143–314. [[CrossRef](#)]
21. Weitkamp, J.; Puppe, L. (Eds.) *Catalysis and Zeolites: Fundamentals and Applications*; Springer: Berlin/Heidelberg, Germany, 1999.
22. Weissenberger, T.; Machoke, A.G.F.; Reiprich, B.; Schwieger, W. Preparation and Potential Catalytic Applications of Hierarchically Structured Zeolites with Macropores. *Adv. Mater. Interfaces* **2021**, *8*, 2001653. [[CrossRef](#)]
23. Petranovskii, V.; Marzke, R.; Diaz, G.; Gómez, A.; Bogdanchikova, N.; Fuentes, S.; Katada, N.; Pestryakov, A.; Gurin, V. Characterization of H and Cu mordenites with varying SiO<sub>2</sub>/Al<sub>2</sub>O<sub>3</sub> ratios, by optical spectroscopy, MAS NMR of <sup>29</sup>Si, <sup>27</sup>Al and <sup>1</sup>H, temperature programmed desorption and catalytic activity for nitrogen oxide reduction. *Stud. Surf. Sci. Catal.* **2002**, *142*, 815–822. [[CrossRef](#)]
24. Wang, M.; Huang, S.; Lü, J.; Cheng, Z.; Li, Y.; Wang, S.; Ma, X. Modifying the acidity of H-MOR and its catalytic carbonylation of dimethyl ether. *Chin. J. Catal.* **2016**, *37*, 1530–1537. [[CrossRef](#)]
25. Lu, K.; Huang, J.; Ren, L.; Li, C.; Guan, Y.; Hu, B.; Xu, H.; Jiang, J.; Ma, Y.; Wu, P. High Ethylene Selectivity in Methanol-to-Olefin (MTO) Reaction over MOR-Zeolite Nanosheets. *Angew. Chem. Int. Ed.* **2020**, *59*, 6258–6262. [[CrossRef](#)] [[PubMed](#)]
26. Hancsók, J.; Kasza, T.; Visnyei, O. Isomerization of n-C<sub>5</sub>/C<sub>6</sub> Bioparaffins to Gasoline Components with High Octane Number. *Energies* **2020**, *13*, 1672. [[CrossRef](#)]
27. Bateni, H.; Able, C. Development of Heterogeneous Catalysts for Dehydration of Methanol to Dimethyl Ether: A Review. *Catal. Ind.* **2019**, *11*, 7–33. [[CrossRef](#)]
28. Sánchez-López, P.; Kotolevich, Y.; Khramov, E.; Chowdari, R.K.; Estrada, M.A.; Berlier, G.; Zubavichus, Y.; Fuentes, S.; Petranovskii, V.; Chávez-Rivas, F. Properties of Iron-Modified-by-Silver Supported on Mordenite as Catalysts for NO<sub>x</sub> Reduction. *Catalysts* **2020**, *10*, 1156. [[CrossRef](#)]
29. Campa, M.C.; Pietrogioacomi, D.; Occhiuzzi, M. The simultaneous selective catalytic reduction of N<sub>2</sub>O and NO<sub>x</sub> with CH<sub>4</sub> on Co- and Ni-exchanged mordenite. *Appl. Catal. B: Environ.* **2015**, *168–169*, 293–302. [[CrossRef](#)]
30. Sugi, Y. Shape-selective alkylation of biphenyl catalyzed by H-Mordenites. *Korean J. Chem. Eng.* **2000**, *17*, 1–11. [[CrossRef](#)]
31. Sugi, Y.; Anand, C.; Subramaniam, V.P.; Stalin, J.; Choy, J.-H.; Cha, W.S.; Elzatahry, A.A.; Tamada, H.; Komura, K.; Vinu, A. The isopropylation of naphthalene with propene over H-mordenite: The catalysis at the internal and external acid sites. *J. Mol. Catal. A: Chem.* **2014**, *395*, 543–552. [[CrossRef](#)]
32. Petranovskii, V.; Pestryakov, A.; Hernández, M.; Rivas, F.C.; Claverie, A.L.; Fuentes, S. Hydrophilicity of Mordenites with Different SiO<sub>2</sub>/Al<sub>2</sub>O<sub>3</sub> Molar Ratio. *Procedia Chem.* **2015**, *15*, 72–78. [[CrossRef](#)]
33. Xie, Z.; Liu, Z.; Wang, Y.; Yang, Q.; Xu, L.; Ding, W. An Overview of Recent Development in Composite Catalysts from Porous Materials for Various Reactions and Processes. *Int. J. Mol. Sci.* **2010**, *11*, 2152–2187. [[CrossRef](#)]
34. Lukyanov, D.B.; Vazhnova, T.; Cherkasov, N.; Casci, J.L.; Birtill, J.J. Insights into Brønsted Acid Sites in the Zeolite Mordenite. *J. Phys. Chem. C* **2014**, *118*, 23918–23929. [[CrossRef](#)]
35. Zhukov, Y.; Efimov, A.Y.; Shelyapina, M.; Petranovskii, V.; Zhizhin, E.; Burovikhina, A.; Zvereva, I. Effect of preparation method on the valence state and encirclement of copper exchange ions in mordenites. *Microporous Mesoporous Mater.* **2016**, *224*, 415–419. [[CrossRef](#)]
36. Zhukov, Y.; Shelyapina, M.; Zvereva, I.; Efimov, A.; Petranovskii, V. Microwave assisted versus convention Cu<sup>2+</sup> exchange in mordenite. *Microporous Mesoporous Mater.* **2018**, *259*, 220–228. [[CrossRef](#)]
37. Shelyapina, M.; Gurgul, J.; Łatka, K.; Sánchez-López, P.; Bogdanov, D.; Kotolevich, Y.; Petranovskii, V.; Fuentes, S. Mechanism of formation of framework Fe<sup>3+</sup> in bimetallic Ag-Fe mordenites—Effective catalytic centers for deNO<sub>x</sub> reaction. *Microporous Mesoporous Mater.* **2019**, *299*, 109841. [[CrossRef](#)]
38. Kalvachev, Y.; Todorova, T.; Popov, C. Recent Progress in Synthesis and Application of Nanosized and Hierarchical Mordenite—A Short Review. *Catalysts* **2021**, *11*, 308. [[CrossRef](#)]
39. Krylova, E.A.; Shelyapina, M.G.; Mazur, A.; Baranov, D.A.; Tsyganenko, A.A.; Petranovskii, V.P. Local Structure of Protonated Mordenites with SiO<sub>2</sub>/Al<sub>2</sub>O<sub>3</sub> ≈ 15 Probed by Multinuclear NMR. *J. Struct. Chem.* **2022**, *63*, 930–943. [[CrossRef](#)]
40. Zhukov, Y.M.; Shelyapina, M.G.; Efimov, A.Y.; Zhizhin, E.V.; Petranovskii, V. Recognition of depth composition profiles of copper-exchanged mordenites applying analytical methods with different depth vision. *Mater. Chem. Phys.* **2019**, *236*, 121787. [[CrossRef](#)]
41. Vicanek, M. Electron transport processes in reflection electron energy loss spectroscopy (REELS) and X-ray photoelectron spectroscopy (XPS). *Surf. Sci.* **1999**, *440*, 1–40. [[CrossRef](#)]

42. Goldstein, J.; Newbury, D.E.; Joy, D.C.; Lyman, C.E.; Echlin, P.; Lifshin, E.; Sawyer, L.; Michael, J.R. *Scanning Electron Microscopy and X-ray Microanalysis*, 3rd ed.; Springer: New York, NY, USA, 2003.
43. Shelyapina, M.G.; Krylova, E.A.; Zhukov, Y.M.; Zvereva, I.A.; Rodriguez-Iznaga, I.; Petranovskii, V.; Fuentes-Moyado, S. Comprehensive Analysis of the Copper Exchange Implemented in Ammonia and Protonated Forms of Mordenite Using Microwave and Conventional Methods. *Molecules* **2019**, *24*, 4216. [[CrossRef](#)]
44. Krylova, E.; Shelyapina, M.; Nowak, P.; Harańczyk, H.; Chislov, M.; Zvereva, I.; Privalov, A.; Becher, M.; Vogel, M.; Petranovskii, V. Mobility of water molecules in sodium- and copper-exchanged mordenites: Thermal analysis and  $^1\text{H}$  NMR study. *Microporous Mesoporous Mater.* **2018**, *265*, 132–142. [[CrossRef](#)]
45. Zhukov, Y.; Kovalyov, A.N.; Kultaeva, A.Y.; Shelyapina, M.; Petranovskii, V. A comparative analysis of the protonated and copper exchanged mordenites with  $\text{SiO}_2/\text{Al}_2\text{O}_3$  molar ratio equal to 10. *Int. J. Nanotechnol.* **2016**, *13*, 136. [[CrossRef](#)]
46. Chen, K.; Gan, Z.; Horstmeier, S.; White, J.L. Distribution of Aluminum Species in Zeolite Catalysts:  $^{27}\text{Al}$  NMR of Framework, Partially-Coordinated Framework, and Non-Framework Moieties. *J. Am. Chem. Soc.* **2021**, *143*, 6669–6680. [[CrossRef](#)] [[PubMed](#)]
47. Shelyapina, M.; Kasperovich, V.; Wolfers, P. Electronic structure and electric-field-gradients distribution in  $\text{Y}_3\text{Al}_5\text{O}_{12}$ : An ab initio study. *J. Phys. Chem. Solids* **2006**, *67*, 720–724. [[CrossRef](#)]
48. Kolodziejski, W.; Barrie, P.J.; He, H.; Klinowski, J. Two-dimensional J-scaled  $^{29}\text{Si}$  NMR COSY of highly siliceous mordenite. *J. Chem. Soc. Chem. Commun.* **1991**, 961–962. [[CrossRef](#)]
49. Fyfe, C.A.; Feng, Y.; Grondey, H.; Kokotailo, G.T.; Gies, H. One- and two-dimensional high-resolution solid-state NMR studies of zeolite lattice structures. *Chem. Rev.* **1991**, *91*, 1525–1543. [[CrossRef](#)]
50. Loewenstein, W. The distribution of aluminum in the tetrahedra of silicates and aluminates. *Am. Mineral.* **1954**, *39*, 92–96.
51. Antúnez-García, J.; Galván, D.; Petranovskii, V.; Murrieta-Rico, F.N.; Yocupicio-Gaxiola, R.I.; Shelyapina, M.G.; Fuentes-Moyado, S. Aluminum distribution in mordenite-zeolite framework: A new outlook based on density functional theory calculations. *J. Solid State Chem.* **2021**, *306*, 122725. [[CrossRef](#)]
52. Glaser, R.H.; Wilkes, G.L.; Bronnimann, C.E. Solid-state  $^{29}\text{Si}$  NMR of TEOS-based multifunctional sol-gel materials. *J. Non-Cryst. Solids* **1989**, *113*, 73–87. [[CrossRef](#)]
53. Shelyapina, M.G.; Yocupicio-Gaxiola, R.I.; Zhelezniak, I.V.; Chislov, M.V.; Antúnez-García, J.; Murrieta-Rico, F.N.; Galván, D.H.; Petranovskii, V.; Fuentes-Moyado, S. Local Structures of Two-Dimensional Zeolites—Mordenite and ZSM-5—Probed by Multinuclear NMR. *Molecules* **2020**, *25*, 4678. [[CrossRef](#)]
54. Shelyapina, M.G.; Silyukov, O.I.; Lushpinskaia, I.P.; Kurnosenko, S.A.; Mazur, A.S.; Shenderovich, I.G.; Zvereva, I.A. NMR Study of Intercalates and Grafted Organic Derivatives of  $\text{H}_2\text{La}_2\text{Ti}_3\text{O}_{10}$ . *Molecules* **2020**, *25*, 5229. [[CrossRef](#)]
55. Xu, M.; Harris, K.D.; Thomas, J.M. In situ solid-state  $^1\text{H}$  NMR studies of hydration of the solid acid catalyst ZSM-5 in its ammonium form. *Solid State Nucl. Magn. Reson.* **2009**, *35*, 93–99. [[CrossRef](#)]
56. Heeribout, L.; Dorémieux-Morin, C.; Nogier, J.-P.; Vincent, R.; Fraissard, J. Study of high-silica H-ZSM-5 acidity by  $^1\text{H}$  NMR techniques using water as base. *Microporous Mesoporous Mater.* **1998**, *24*, 101–112. [[CrossRef](#)]
57. Huo, H.; Peng, L.; Grey, C.P. Low Temperature  $^1\text{H}$  MAS NMR Spectroscopy Studies of Proton Motion in Zeolite HZSM-5. *J. Phys. Chem. C* **2009**, *113*, 8211–8219. [[CrossRef](#)]
58. Shelyapina, M.G.; Silyukov, O.I.; Andronova, E.A.; Nefedov, D.Y.; Antonenko, A.O.; Missyul, A.; Kurnosenko, S.A.; Zvereva, I.A.  $^1\text{H}$  NMR Study of the  $\text{HCa}_2\text{Nb}_3\text{O}_{10}$  Photocatalyst with Different Hydration Levels. *Molecules* **2021**, *26*, 5943. [[CrossRef](#)] [[PubMed](#)]
59. Shelyapina, M.G.; Nefedov, D.Y.; Kostromin, A.V.; Silyukov, O.I.; Zvereva, I.A. Proton mobility in Ruddlesden–Popper phase  $\text{H}_2\text{La}_2\text{Ti}_3\text{O}_{10}$  studied by  $^1\text{H}$  NMR. *Ceram. Int.* **2018**, *45*, 5788–5795. [[CrossRef](#)]
60. Cattaneo, A.S.; Ferrara, C.; Marculescu, A.M.; Giannici, F.; Martorana, A.; Mustarelli, P.; Tealdi, C. Solid-state NMR characterization of the structure and thermal stability of hybrid organic–inorganic compounds based on a  $\text{HLaNb}_2\text{O}_7$  Dion–Jacobson layered perovskite. *Phys. Chem. Chem. Phys.* **2016**, *18*, 21903–21912. [[CrossRef](#)]
61. Essayem, N.; Tong, Y.Y.; Jobic, H.; Vedrine, J.C. Characterization of protonic sites in  $\text{H}_3\text{PW}_{12}\text{O}_{40}$  and  $\text{Cs}_{1.9}\text{H}_{1.1}\text{PW}_{12}\text{O}_{40}$ : A solid-state  $^1\text{H}$ ,  $^2\text{H}$ ,  $^{31}\text{P}$  MAS-NMR and inelastic neutron scattering study on. *Appl. Catal. A Gen.* **2000**, *194–195*, 109–122. [[CrossRef](#)]
62. Hronský, V. Measurement of Sample Temperatures and Temperature Gradients in Magic-Angle Spinning Nmr. *Acta Electrotech. et Inform.* **2013**, *13*, 95–98. [[CrossRef](#)]
63. Yesinowski, J.P.; Ladouceur, H.D.; Purdy, A.P.; Miller, J. Electrical and ionic conductivity effects on magic-angle spinning nuclear magnetic resonance parameters of  $\text{CuI}$ . *J. Chem. Phys.* **2010**, *133*, 234509. [[CrossRef](#)]
64. Losch, P.; Joshi, H.; Stegmann, N.; Vozniuk, O.; Schmidt, W. Studying Proton Mobility in Zeolites by Varying Temperature Infrared Spectroscopy. *Molecules* **2019**, *24*, 3199. [[CrossRef](#)]
65. Katsiotis, M.S.; Fardis, M.; Al Wahedi, Y.; Stephen, S.; Tzitzios, V.; Boukos, N.; Kim, H.J.; Alhassan, S.M.; Papavassiliou, G. Water Coordination, Proton Mobility, and Lewis Acidity in HY Nanozeolites: A High-Temperature  $^1\text{H}$  and  $^{27}\text{Al}$  NMR Study. *J. Phys. Chem. C* **2015**, *119*, 3428–3438. [[CrossRef](#)]
66. Tsyganenko, A.A.; Kondratieva, E.V.; Yanko, V.S.; Storozhev, P.Y. FTIR study of CO adsorption on basic zeolites. *J. Mater. Chem.* **2006**, *16*, 2358–2363. [[CrossRef](#)]
67. Morterra, C.; Magnacca, G. A case study: Surface chemistry and surface structure of catalytic aluminas, as studied by vibrational spectroscopy of adsorbed species. *Catal. Today* **1996**, *27*, 497–532. [[CrossRef](#)]

68. Hadjiivanov, K.I.; Vayssilov, G.N. Characterization of oxide surfaces and zeolites by carbon monoxide as an IR probe molecule. *Adv. Catal.* **2002**, *47*, 307–511.
69. Kondratieva, E.V.; Manoilova, O.V.; Tsyganenko, A.A. Integrated absorption coefficient of adsorbed CO. *Kinet. Catal.* **2008**, *49*, 451–456. [[CrossRef](#)]
70. Bulanin, K.M.; Mikheleva, A.Y.; Shchepkin, D.N.; Rudakova, A.V. Determination of the Extinction Coefficient of Carbon Monoxide Adsorbed on Titanium Dioxide. *Opt. Spectrosc.* **2022**, *130*, 248–256. [[CrossRef](#)]
71. Gabrienko, A.A.; Danilova, I.G.; Arzumanov, S.S.; Pirutko, L.V.; Freude, D.; Stepanov, A.G. Direct Measurement of Zeolite Brønsted Acidity by FTIR Spectroscopy: Solid-State  $^1\text{H}$  MAS NMR Approach for Reliable Determination of the Integrated Molar Absorption Coefficients. *J. Phys. Chem. C* **2018**, *122*, 25386–25395. [[CrossRef](#)]
72. Henriques, C.; Marie, O.; Thibault-Starzyk, F.; Lavalley, J.-C.  $\text{NO}^+$  ions as IR probes for the location of OH groups and  $\text{Na}^+$  ions in main channels and side pockets of mordenite. *Microporous Mesoporous Mater.* **2001**, *50*, 167–171. [[CrossRef](#)]
73. Marie, O.; Massiani, P.; Thibault-Starzyk, F. Infrared Evidence of a Third Brønsted Site in Mordenites. *J. Phys. Chem. B* **2004**, *108*, 5073–5081. [[CrossRef](#)]
74. Tsyganenko, A.A. Variable Temperature IR Spectroscopy in the Studies of Oxide Catalysts. *Top. Catal.* **2013**, *56*, 905–913. [[CrossRef](#)]
75. Levantovsky, A. *MagicPlot 3.0.0*; Magicplot Systems, LLC.: St. Petersburg, Russia, 2021; Available online: <https://magicplot.com/> (accessed on 23 December 2022).

**Disclaimer/Publisher’s Note:** The statements, opinions and data contained in all publications are solely those of the individual author(s) and contributor(s) and not of MDPI and/or the editor(s). MDPI and/or the editor(s) disclaim responsibility for any injury to people or property resulting from any ideas, methods, instructions or products referred to in the content.